NAVAL POSTGRADUATE SCHOOL

MONTEREY, CALIFORNIA

THESIS

FEASIBILITY OF UNDERWATER LIDAR TECHNOLOGY FOR BOTTOM SENSING

by

Jacob T. Dwyer

September 2023

Co-Advisors: Joseph A. Blau
Keith R. Cohn

THIS PAGE INTENTIONALLY LEFT BLANK

REPORT DOCUMENTATION PAGE	*Form Approved OMB No. 0704-0188*

1. AGENCY USE ONLY *(Leave blank)*	**2. REPORT DATE** September 2023	**3. REPORT TYPE AND DATES COVERED** Master's thesis

4. TITLE AND SUBTITLE FEASIBILITY OF UNDERWATER LIDAR TECHNOLOGY FOR BOTTOM SENSING	**5. FUNDING NUMBERS**
6. AUTHOR(S) Jacob T. Dwyer	
7. PERFORMING ORGANIZATION NAME(S) AND ADDRESS(ES) Naval Postgraduate School Monterey, CA 93943-5000	**8. PERFORMING ORGANIZATION REPORT NUMBER**
9. SPONSORING / MONITORING AGENCY NAME(S) AND ADDRESS(ES) NIWC, San Diego, CA 53560	**10. SPONSORING / MONITORING AGENCY REPORT NUMBER**

11. SUPPLEMENTARY NOTES The views expressed in this thesis are those of the author and do not reflect the official policy or position of the Department of Defense or the U.S. Government.

12a. DISTRIBUTION / AVAILABILITY STATEMENT Approved for public release. Distribution is unlimited.	**12b. DISTRIBUTION CODE** A

13. ABSTRACT (maximum 200 words)

Lasers have been used for several decades to perform multiple functions in areas such as communication, detection, and imaging. Only recently have lasers been used to operate in the navigational realm, particularly for land vehicles such as self-driving cars. This technology has not been used to a wide extent under the surface of the ocean, however, due to the high scattering and absorption properties of seawater. Very little research on laser propagation has been done in areas of the ocean such as below the euphotic zone where the absorption of light is minimized due to the lack of organic material. This paper assesses the feasibility of lasers to be used for underwater navigational purposes and act as an alternative to existing bathymetric sensing devices. This is done by creating a computer model based on the Beer-Lambert law and the general lidar equation. Additionally, the stealth capabilities of a laser bathymetric device is discussed.

14. SUBJECT TERMS LIDAR, laser, navigation, undersea warfare, submarines, undersea navigation, undersea sensing, sensors	**15. NUMBER OF PAGES** 75
	16. PRICE CODE

17. SECURITY CLASSIFICATION OF REPORT Unclassified	**18. SECURITY CLASSIFICATION OF THIS PAGE** Unclassified	**19. SECURITY CLASSIFICATION OF ABSTRACT** Unclassified	**20. LIMITATION OF ABSTRACT** UU

NSN 7540-01-280-5500

Standard Form 298 (Rev. 2-89)
Prescribed by ANSI Std. 239-18

THIS PAGE INTENTIONALLY LEFT BLANK

Approved for public release. Distribution is unlimited.

FEASIBILITY OF UNDERWATER LIDAR TECHNOLOGY FOR BOTTOM SENSING

Jacob T. Dwyer
Lieutenant, United States Navy
BA, Arizona State University, Tempe, 2016

Submitted in partial fulfillment of the
requirements for the degree of

MASTER OF SCIENCE IN APPLIED PHYSICS

from the

NAVAL POSTGRADUATE SCHOOL
September 2023

Approved by: Joseph A. Blau
Co-Advisor

Keith R. Cohn
Co-Advisor

Frank A. Narducci
Chair, Department of Physics

THIS PAGE INTENTIONALLY LEFT BLANK

ABSTRACT

Lasers have been used for several decades to perform multiple functions in areas such as communication, detection, and imaging. Only recently have lasers been used to operate in the navigational realm, particularly for land vehicles such as self-driving cars. This technology has not been used to a wide extent under the surface of the ocean, however, due to the high scattering and absorption properties of seawater. Very little research on laser propagation has been done in areas of the ocean such as below the euphotic zone where the absorption of light is minimized due to the lack of organic material. This paper assesses the feasibility of lasers to be used for underwater navigational purposes and act as an alternative to existing bathymetric sensing devices. This is done by creating a computer model based on the Beer-Lambert law and the general lidar equation. Additionally, the stealth capabilities of a laser bathymetric device is discussed.

THIS PAGE INTENTIONALLY LEFT BLANK

TABLE OF CONTENTS

I. INTRODUCTION 1

A. DESCRIPTION OF THESIS 1
B. THESIS OBJECTIVE AND SCOPE 2

II. BACKGROUND INFORMATION 5

A. HISTORY OF LIDAR AND INSPIRATION OF THESIS 5
B. LIDAR TECHNOLOGY AND THE ENVIRONMENT 6
1. Scattering 7
2. Absorption 9
3. Water Classification and Description of Water Column 13
C. THE UNDERWATER LIDAR EQUATION 15
1. Laser Output Energy 16
2. Spectral Transmission Factor 17
3. Transmission Factor 17
4. Geometrical Factor and Receiver Optics Factor 18
5. Backscattering Coefficient 21
6. Detector Operation Factor 23
7. Background Radiation Power 23

III. DATABASES AND METHODOLOGY 25

A. NAVAL INFORMATION WARFARE CENTER DATA 25
B. WORLDWIDE OCEAN OPTICS DATABASE 26
C. METHODOLOGY 26

IV. MODELING RESULTS 33

A. RESULTS USING NIWC DATA 33
1. Fall. Vehicle at 20, 80 m. Safety Standoff Range at 10 m and 30 m. 33
2. Spring. Vehicle at 20, 80 m. Safety Standoff Range at 10 m and 30 m. 38
3. A Note on NIWC Summer Data 42
B. RESULTS USING WOOD DATA 42
1. Sea of Japan 42
2. East China Sea 45
C. A NOTE ON DETECTABILITY OF LIDAR SIGNAL BY ADVERSARIES 48

V. CONCLUSION AND FUTURE WORK 51

APPENDIX. NIWC SUMMER DATA 53

LIST OF REFERENCES 55

INITIAL DISTRIBUTION LIST 57

LIST OF FIGURES

Figure 1. Log-linear plot of VSF, laser source: 515 nm. The VSF describes the distribution of scattered power from an incoming beam of light across individual scattering angles. Source: [3] 9

Figure 2. Pure water absorption curve based on wavelength of incoming light. Source: [4] 10

Figure 3. Comparing the difference between idealized open ocean absorption spectra (top) and coastal ocean absorption spectra (bottom). Source: [3] 13

Figure 4. Transmission of radiation based on Jerlov Water Classification. Source: [3] 15

Figure 5. Simple overlap factor. Source: [8] 19

Figure 6. Example of an offset lidar configuration, red indicates laser diameter, blue indicates acceptance range of detector. 20

Figure 7. Results of simple overlap factor changing with depth in an example system configuration. 21

Figure 8. Map of data locations used by the worldwide ocean optics database (WOOD). 28

Figure 9. Geometry of the simulations in the MATLAB script. 31

Figure 10. NIWC fall data: attenuation vs. depth, wavelength: 470nm. Vehicle depths of 20 m and 80 m indicated by asterisks. 35

Figure 11. Received photon count vs. seafloor depth, using NIWC fall data. Vehicle depth at 20 m, safety standoff range is 10 m and 30 m. 35

Figure 12. Received photon count vs. seafloor depth, using NIWC fall data. Vehicle depth at 80 m, safety standoff range is 10 m and 30 m. 37

Figure 13. Maximum detectable depth below keel vs. vehicle depth, using NIWC fall data. 38

Figure 14. NIWC spring data: attenuation vs. depth, wavelength: 470 nm. Vehicle depths of 20 m and 80 m indicated by asterisks. 39

Figure 15. Received photon count vs. seafloor depth, using NIWC spring data. Vehicle depth at 20 m, safety standoff range is 10 m and 30 m. 40

Figure 16. Received photon count vs. seafloor depth, using NIWC spring data. Vehicle depth at 80 m, safety standoff range is 10 m and 30 m. 40

Figure 17. Maximum detectable depth below keel vs. vehicle depth, using NIWC spring data. 41

Figure 18. WOOD data, Sea of Japan: attenuation vs. depth 43

Figure 19. Received photon count vs. seafloor depth, using WOOD data. Sea of Japan. Vehicle depth at 20 m. 44

Figure 20. Received photon count vs. seafloor depth, using WOOD data. Sea of Japan. Vehicle depth at 80 m. 44

Figure 21. Maximum detectable depth below keel vs. vehicle depth, using WOOD data, Sea of Japan. 45

Figure 22. WOOD data, East China Sea: attenuation vs. depth. 46

Figure 23. Received photon count vs. seafloor depth, using WOOD data. East China Sea. Vehicle depth at 20 m. 47

Figure 24. Received photon count vs. seafloor depth, using WOOD data. East China Sea. Vehicle depth at 80 m. 47

Figure 25. Maximum detectable depth below keel vs. vehicle depth, using WOOD data, East China Sea. 48

Figure 26. NIWC-provided attenuation data, summer 53

Figure 27. NIWC-provided photon count data, summer 53

LIST OF TABLES

Table 1. Input values for general lidar equation model 29

THIS PAGE INTENTIONALLY LEFT BLANK

LIST OF ACRONYMS AND ABBREVIATIONS

CDOM	colored dissolved organic matter
FOV	field of view
LIDAR	light detection and ranging
NASA	National Aeronautics and Space Administration
NIWC	Naval Information Warfare Center
NOAA	National Oceanic and Atmospheric Administration
PAR	photosynthetically available radiation
SONAR	sound detection and ranging
UUV	unmanned underwater vehicle
VSF	volume scattering function
WOOD	Worldwide Ocean Optics Database

THIS PAGE INTENTIONALLY LEFT BLANK

ACKNOWLEDGMENTS

I would like to thank my advisors, Dr. Keith Cohn and Dr. Joseph Blau for their hard work, insight, and mentorship throughout writing this thesis and Brittany, who sacrificed a lot to ensure this process went smoothly.

THIS PAGE INTENTIONALLY LEFT BLANK

I. INTRODUCTION

Submarine and unmanned underwater vehicle (UUV) navigation currently includes using sonar, charts, and/or pre-programmed routes to verify position and to avoid collision with underwater hazards. This thesis focuses on determining the feasibility of using laser technology, in the form of a process called light detection and ranging (LIDAR), to supplement the current navigational tools in shallow, coastal waters. Additionally, the thesis discusses limitations of laser technology, the potential of counter detection of the system described in this thesis, and future applications in which lasers could be used to supplement other mission focus areas for these underwater vehicles.

A. DESCRIPTION OF THESIS

Submarines have been a critical part of the modern Navy for over a century, and in the past decade an increased focus on UUVs has begun to take place as well. Both systems use a combination of sound for navigation, in the form of sonar technology, because visibility is poor at the depth of vehicle operation. Due to this, submarines and UUVs are essentially "blind" and can only navigate by listening to the surrounding noise and projecting the vehicle position using potentially outdated charts. This can lead to occupational hazards and, in some cases, collision incidents. Additionally, since depth-sensing bathometers release sound energy into the surrounding waters, an elevated risk of counter detection exists in areas where these vehicles perform missions. With these limitations in mind, there exists a need for a specific technology that can provide a solution to this problem, which is the motivation for this thesis: optical navigation using lidar.

Lidar technology uses lasers to sense seafloor depth at a near-instantaneous rate, supplying close-to-real-time sensing of the seafloor and any navigational hazards that may exist in the path of these underwater vehicles. Additionally, lasers are much harder to detect than sonar technologies, as the energy they radiate does not propagate far through the water column, which reduces the possibility of counter detection. Depending on the type of sound and the propagation paths available to it, sound can travel several

kilometers. Lasers on the other hand might only propagate within one kilometer in the most ideal of conditions. Adversaries would also have to carry optical detectors and would have to be close to detect any optical emissions from the underwater vehicles. Even if a detector detected the laser beam, the adversary would need to analyze the data to prove it came from a submarine. This could be difficult as the lidar operates in the visible spectrum of light, so the adversary would need to discriminate the laser signal from the scattered sunlight in the upper ocean. The scattered sunlight would contain many photons of the same wavelength as the emitted light from the underwater vessel, which would therefore raise the noise floor enough to make the return from the bottom much harder to detect.

However, the shorter propagation distance of the lidar signal is also the technology's biggest limitation: lasers do not propagate well in ocean water and thus the ranges at which they work are limited to short, near-vehicle distances. Lasers, at the technology's current ability and power, are unable to reach and sense deep seafloors. Scattering and absorption of the light attenuates the laser beam rapidly, and thus lasers are unable to be used fully as a replacement to depth-sensing sonar technologies. This limitation raises questions that this thesis tries to answer: what is the deepest point from the bottom of an underwater vehicle that a laser can sense and how feasible is it for an underwater vehicle to use this as a primary navigational tool in littoral environments?

B. THESIS OBJECTIVE AND SCOPE

The objective of this thesis is to investigate the limitations of underwater lidar navigation, including the best operation depths of this technology and the information it provides to the vehicles that use it. This is done by developing a computational model based on the Beer-Lambert law and the general version of the lidar equation to calculate the attenuation of light in the ocean environment. The model uses parameters from an established optical oceanography database to supply realistic results. Several data sources from around the world at different total depths and water types are used to generalize a relative maximum operating depth of lidar systems at various wavelengths, power outputs, and locations.

In Chapter II, a history of lidar technology is briefly discussed, including its current applications in airborne lidar platforms and how those contribute to the research discussed in this thesis. Additionally, a technical description of lidar technology, the lidar equation, and the Beer-Lambert law is discussed. Underwater laser propagation follows from the aforementioned discussions to further develop a background in the ranges that lasers can propagate through water. Finally, a discussion on water types, the water column zones, and environmental trends within the column finishes the chapter to fully integrate the proper knowledge into the developed model.

Chapter III discusses the underwater laser propagation model to explore the potential benefits and limitations of underwater laser navigation. Additionally, the databases used for the proceeding results section is discussed including data collection techniques and background information.

In Chapter IV, the results of using the model with established data is discussed. Underwater propagation data from selected databases are used to validate the limitations of the model discussed in the previous chapter. Finally, a conclusion is drawn in Chapter V that generalizes the limitations of the model and future opportunities to further research the topic is provided.

THIS PAGE INTENTIONALLY LEFT BLANK

II. BACKGROUND INFORMATION

Like the related concept of sonar, lidar is an acronym that stands for "Light Detection and Ranging" and is similarly written in lowercase. Lidar technology has been used for decades for remote sensing applications and more recently for navigation applications. This technology uses light pulses to detect an object of interest and then use the result to calculate and report on the range to the object. Since coherent laser sources supply much more radiance than incoherent light sources, lasers were immediately considered to be the best choice for this technology. This chapter serves as an introduction to the science and operation of lidar technology and will discuss the general lidar equation along with its extension to the underwater environment.

A. HISTORY OF LIDAR AND INSPIRATION OF THESIS

Beginning in the 1960s, lasers began to be used in many functions other than novelty and pure physics research. The invention of the first lidar system is commonly attributed to the Hughes Aircraft Company in 1961 [1], shortly after the invention of the laser in 1960, with the express purpose of tracking satellites. Meteorology applications began shortly thereafter by a multitude of organizations to track and map weather patterns and objects like clouds and pollution. Perhaps the most well-known application of lidar-type technology is from the 1970s when the Apollo 15 mission mapped the surface of the moon using a laser altimeter which functions in a similar manner. As technology progressed and lidar systems became more powerful and efficient, bathymetric mapping and navigation applications began to arise.

One of the more commonly used military applications of lidar is airborne lidar, also known as bathymetric lidar. The concept of using lidar to actively map the seafloor topography of the ocean began in 1969 when Daniel Hickman and John Hogg produced a research paper describing the effectiveness of using a lidar system for this purpose. Depths of approximately 120 ft were recorded in areas of clear water [2]. Since this study was performed, civilian corporations and the military began to consistently use airborne lidar to map coastal seafloor topography. Airborne lidar involves a complex equation that

must include the speed of the aircraft and the several boundary interactions a laser beam experiences as it is transmitted through the air, interacts with the water surface, propagates through the water, and then encounters the same interactions on its return path. These interactions only become more complicated when scattering and absorbing materials present within the water exist in higher concentrations near the water surface. All these complications combine to significantly reduce the overall return signal and thus will restrict the use of lidar to very shallow areas of the ocean.

Considering the effectiveness of lidar as a navigational tool, this thesis investigates the use of lidar as a navigational and safety aid for submarines and UUVs. Several benefits are involved in using a lidar system in this capacity: one main reason is the ability of a laser to concentrate on a certain area within the water column. Additionally, while acting as a bathometer, the return signals could be used to navigate the submarine under certain circumstances. Another benefit of using a subsurface vehicle to host a lidar system is its unique ability to travel into areas of the water column that have less material that attenuates the return signal. This could potentially allow for greater detection depths to be reached by a subsurface bathymetric system than by airborne or surface employed lidar systems.

B. LIDAR TECHNOLOGY AND THE ENVIRONMENT

Lidar technology is a physical application of lasers. The word “laser” is itself an acronym for “light amplification by stimulated emission of radiation”. In a typical laser, a gas, liquid, plasma or solid is energized (usually electrically or optically) in such a way that light is generated in response. The light is then amplified in an optical cavity. Once the laser crosses a certain operating threshold, the light becomes coherent and can be released to perform tasks. Specifically in the case of lidar, this task is to remotely sense an object and return its range for a person or computer to analyze. There are several types of interactions a laser pulse encounters along its travel path that attenuate its signal, including scattering and absorption. This attenuation is then calculated using the Beer-Lambert Law:

$$P_R = P_0 e^{-\int \varepsilon(R)dR}$$

where P_R and P_0 are respectively the received and initial power, R is the range, and ε is the attenuation coefficient, described separately by:

$$\varepsilon = \alpha + \beta$$

where α is the absorption coefficient and β is the backscatter coefficient of the water.

1. Scattering

The scattering of light during propagation through water takes on two forms: elastic and inelastic scattering. Elastic scattering results in no change to the wavelength and is often modeled in two separate ways, Rayleigh scattering and Mie scattering; the choice of models depends on the size of the scatterer relative to the wavelength of light. Rayleigh scattering is appropriate when the scatterers "are much smaller than the wavelength of light" [3]. The alternating electric field of the incoming light induces alternating dipoles in the molecules that then radiate light at the same frequency as the radiation field; this is Rayleigh scattered light. Since lidar uses light within the visible light spectrum, where the wavelengths are much larger (~500 nm) than water molecules (diameter ~0.3 nm), Rayleigh scattering can be considered for interactions with pure water only. However, Rayleigh scattering is inadequate to discuss particles much larger than pure water, such as phytoplankton and other particulate matter.

The second elastic interaction is Mie scattering, which is developed from interactions with larger particulates. An in-depth description of Mie scattering can be found in [4], but a cursory touch on the subject can be found below to familiarize the reader with the concept. Mie theory conceptualizes any size particle suspended in sea water as a material through which light rays can propagate. This allows any type of particle to be generalized by familiar optics concepts such as reflection, diffraction, and refraction. Because this theory incorporates these phenomena, it accurately describes empirical data for the angular distribution of scattered light in sea water samples, as seen in Figure 1. Mie theory itself can predict the same type of scattering as Rayleigh

scattering (indeed, Mie scattering reduces to Rayleigh scattering in the limit where particle size is much smaller than the wavelength) but has the added benefit of being able to model much larger particles, which are actively present within seawater. The Mie scattering calculations are computationally intensive. However, for ease of calculation, Rayleigh scattering is used as a surrogate to model scattering by water molecules. Therefore, in discussions of underwater light scattering, Mie theory will be used to describe scattered light from large particles and Rayleigh scattering will be used to discuss scattering by pure sea water [4].

Further interactions include inelastic mechanisms like Raman scattering, in which a portion of the initial photon energy is lost in the interaction. While this type of scattering does occur in some form, it is commonly regarded in the underwater photonics community that elastic scattering is the dominant interaction, and inelastic interactions occur in significantly less proportions unless the water column contains a significant concentration of absorbing matter, such as phytoplankton or chlorophyll [3], [4]. Additionally, the emitted light that results from Raman scattering has its wavelength shifted in a significant enough way [3] that spectral filters can remove it from the return signal; therefore, Raman scattering will only be considered as an attenuation mechanism for lidar applications.

The angular distribution of scattered light can be visualized in Figure 1. The figure is a product of Petzold's direct measurements in different types of ocean water and present the data in the form of a volume scattering function (VSF), which describes the distribution of scattered power from an incoming beam of light across individual scattering angles [3]. The graphs assist in visualizing how much light is being scattered off-axis, which contributes to the total attenuation of light as it propagates through the water column. In the following figures, three different water types were assessed: a turbid harbor environment, a coastal ocean environment, and a clear ocean environment [5]. Zero degrees represents light that was either forward scattered or not scattered at all. 180 degrees indicates radiation that has been scattered and its resulting path will be in the exact opposite direction of its initial trajectory. All other angles describe the distribution of radiation that has been scattered in some other direction. These measurements show

that after the VSF is normalized (by dividing the function by the scattering coefficient), most of the global waters have an incredibly similar angular distribution of scattered light [3]. The log-linear plot is used to see the overall comparison between the proportion of forward to back scattered light by noting the large peak near zero-degree scattering angle compared to the slight rise near 180-degree scattering angle. This plot visually shows that most of the light continues to propagate in the forward direction (~0 degrees).

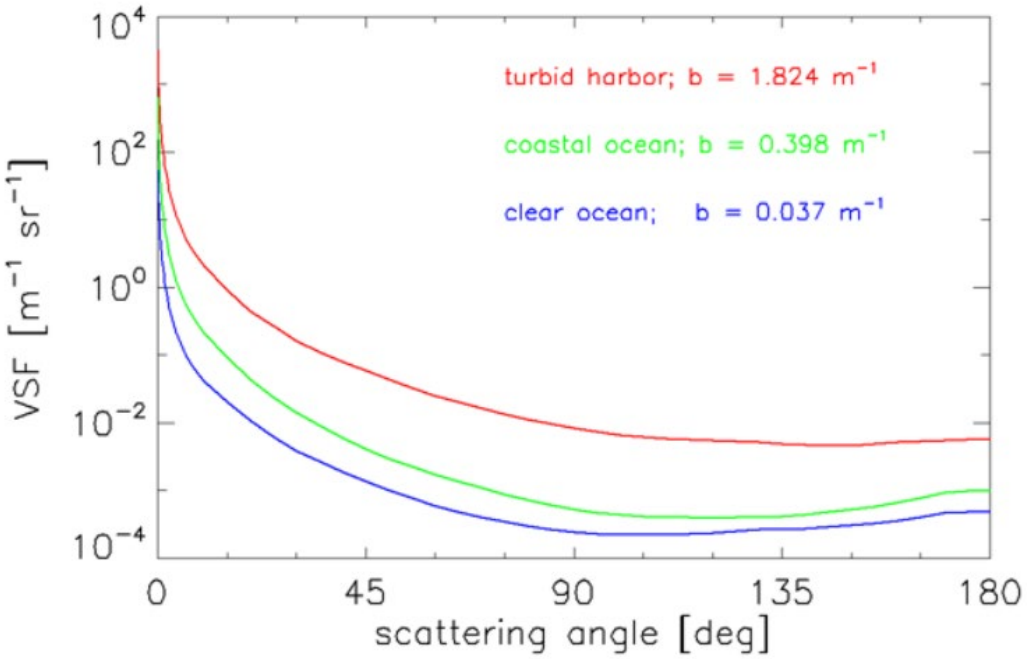

Figure 1. Log-linear plot of VSF, laser source: 515 nm. The VSF describes the distribution of scattered power from an incoming beam of light across individual scattering angles. Source: [3]

2. Absorption

Absorption is the other major attenuation mechanism that light encounters while propagating. Absorption occurs when a photon approaches a molecule and is then subsequently absorbed by the molecule. This will increase the energy state of the molecule by exciting either its vibrational, rotational, or electronic states depending on the energy of the absorbed photon. For visible light lasers, such as those used for

underwater lidar, the energy of the incoming photons is sufficient to raise the electronic energy states of the molecule.

Several major components of sea water affect the strength of attenuation via absorption. These include pure sea water itself, phytoplankton, decomposed plant material, and other inorganic particulates. For pure water, absorption strengths are typically exceptionally low until the upper range of the visible light spectrum. Weak vibrational energy transitions occur up to ~600 nm resulting in low absorption strength. Above 600 nm, stronger vibrational energy transitions then introduce a noticeable and significant rise in absorption strength as seen in Figure 2. The vertical axis in this figure is the absorption coefficient, which is the fraction of incident power absorbed per unit distance (note the scale change at a wavelength of ~720 nm, as indicated by the vertical dashed line).

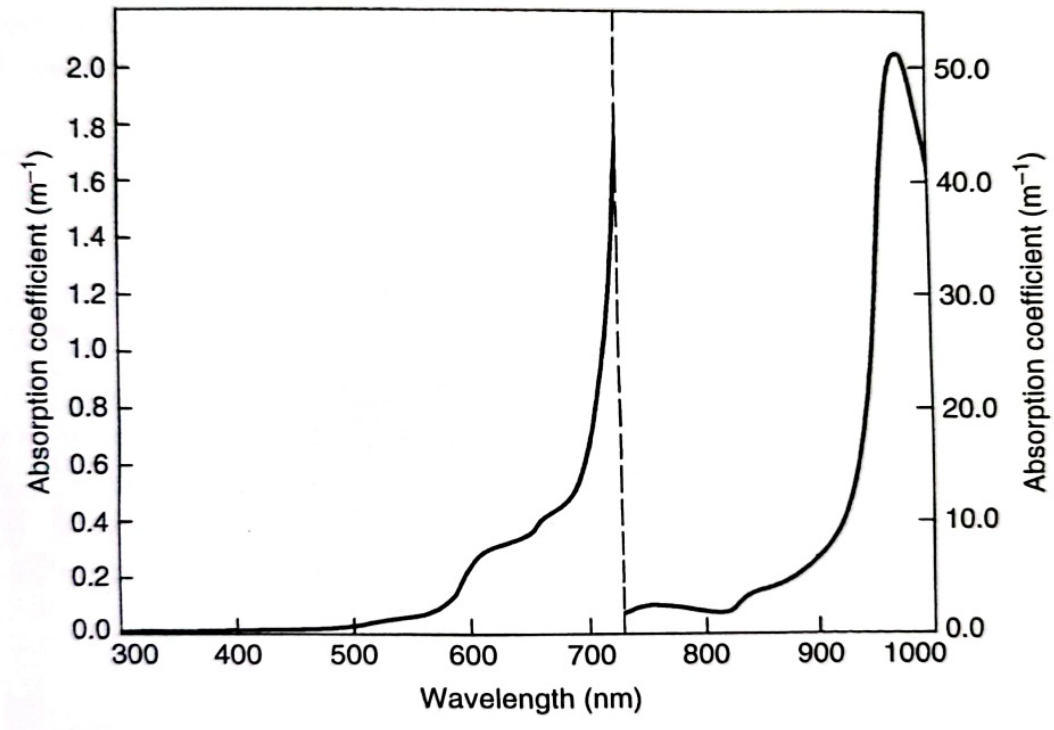

Figure 2. Pure water absorption curve based on wavelength of incoming light. Source: [4]

The introduction of salt at sea water concentrations only causes a very small rise in absorption strength throughout most of the visible spectrum (400 nm to 680 nm), on the order of 0.002 m^{-1} at its maximum absorption strength [6]. This is negligible compared to any other attenuating factor within the water column. Therefore, the absorption by sea water for any given wavelength can be approximated with the absorption by pure water for the same given wavelength.

Phytoplankton and other photosynthesizing materials absorb significantly more light than pure sea water. The main absorbing component of photosynthetic materials is chlorophyll, of which there are two types: chlorophyll a and chlorophyll b. Regardless of type, chlorophyll has two main absorbing bands, one in the red portion of the visible spectrum and one in the blue. While this indicates that chlorophyll will more readily absorb light in these portions of the spectrum, any wavelength of light has a probability to be absorbed. All photons, once absorbed, are removed from the signal and are lost [4]. The absorption strength of photosynthetic materials depends on the location and concentration of chlorophyll within the water. In shallow water areas, photosynthetic materials could span the entire water column from surface to seafloor. In deeper coastal waters or open ocean, the concentration of photosynthetic materials depends on the strength of the ambient light introduced by the sun. Therefore, there are higher concentrations of chlorophyll-holding materials near the surface of the ocean that extend partially into the water column until no ambient light is left, at which point the water is effectively free of the material altogether.

While the transformation of photon energy to heat energy is the major outcome of absorption in photosynthetic materials, fluorescence does occur as well. This occurs after a molecule absorbs a photon and is raised to a higher energy state. Instead of transitioning down to the ground state solely through the energy levels driven by vibrational and rotational energy transfers, a molecule can transition to a lower energy state by emitting a photon of lesser energy than the original. Even though this does occur naturally, fluorescence typically only occurs with ~1% of absorbed light in photosynthetic materials. The vast majority of absorbed light is transformed into biomass and thus

fluorescence in these materials is negligible. Like for Raman scattering, photons produced from fluorescence can be removed with a filter, if desired.

Non-photosynthetic materials such as decomposed plant matter, also known as colored dissolved organic matter (CDOM), and other inorganic particulate matter absorb light in a separate way. After one of these molecules absorbs a photon and its energy state is raised, the absorbed photon is transformed into heat energy and thus contributes to the attenuation of the original signal [4]. The absorption strengths of these types of materials vary widely depending on location. For example, the open ocean does not have a high concentration of these materials, and therefore the absorption strength attributed to these materials are low. However, for coastal and inland waters, the location of nearby rivers, estuaries, or other sources of plant material can significantly raise the overall absorption strength from this component.

The absorption strength of the previously mentioned mechanisms in sea water are quantified in Figure 3, which compares the absorption spectra (absorption coefficient versus wavelength) for open ocean water components against a coastal ocean water environment. There is a significant difference in the lower end of the visible light spectrum between the two types of water driven by chlorophyll and particulate matter, as well as a noticeable increase of absorption strength in the middle of the range. However, it is evident that there is an absorption minimum in the <500nm range in open ocean and in the 500-600nm range for coastal water.

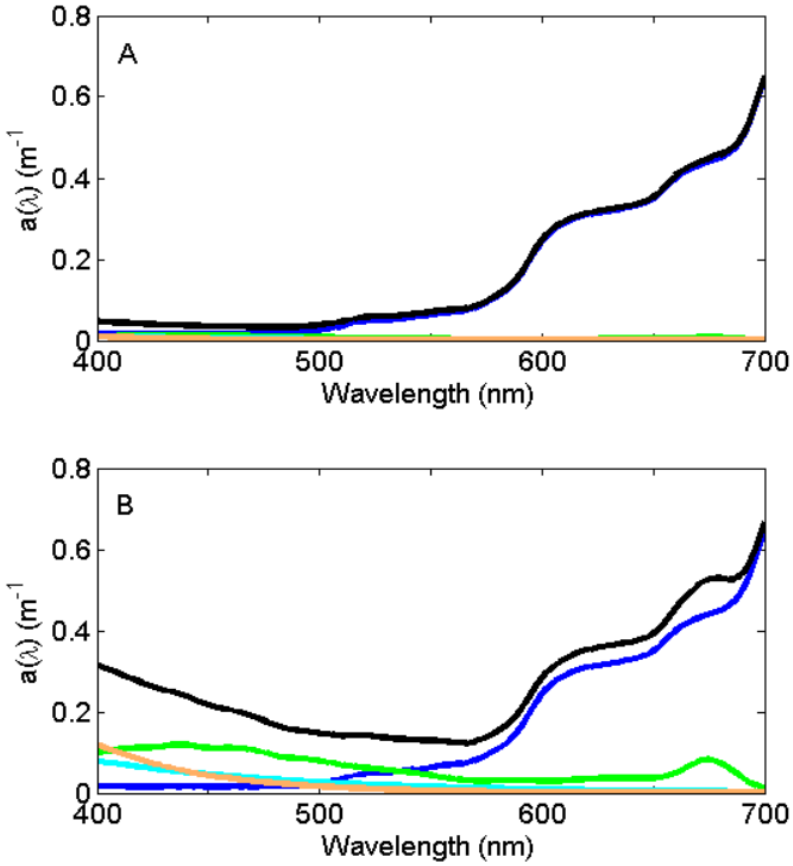

Figure 3. Comparing the difference between idealized open ocean absorption spectra (top) and coastal ocean absorption spectra (bottom). Source: [3]

The dark blue line in Figure 3 indicates the absorption in pure water, the green line indicates absorption done by generic phytoplankton, the light blue line indicates the absorption done by non-algal particulates, the orange line indicates the absorption done by colored dissolved organic matter, and the black line indicates the total absorption done by all the previously described constituents of ocean water.

3. Water Classification and Description of Water Column

Since the scattering and absorbing characteristics of water depend on the concentrations of material suspended in the water, a description of the water column is necessary. The ocean is typically broken up into three regions when describing the natural light field created by the sun: the photic/euphotic zone, the dysphotic zone, and

the aphotic zone. The dysphotic and aphotic zones contain little to no residual sunlight and extend from intermediate to maximum ocean depths. The euphotic zone is the area that receives the vast majority of sunlight; its maximum depth is defined as where ambient sunlight levels reach 1% of its surface levels. Typically, the maximum depth for this zone is around 200 m but can fluctuate based on sunlight availability. The euphotic zone is where the majority of the marine life and photosynthetic materials reside and is thus the region is where the theoretical maximum of light attenuation exists; it is the most important zone when discussing lidar operation [4].

The concentration of phytoplankton and other photosynthetic material drops significantly from the ocean surface to the bottom of the euphotic zone, although in some areas of the world a secondary maximum of chlorophyll concentrations exists at greater depths [3]. In shallow waters that do not completely attenuate sunlight, chlorophyll concentrations could maintain at high levels throughout the water column and cause significant attenuation. CDOM and other detritus concentrations reach elevated levels near-shore in coastal waters and can reach staggering concentrations near estuaries and inside of inland waters. These all affect perceived water clarity and thus the ability of light to propagate through it.

On the topic of water clarity, a description of Jerlov water types is necessary. Jerlov water types describe the ability of radiation to propagate through a particular body of water. For example, open ocean lacks much of the foreign matter of coastal ocean waters, therefore, light will more easily propagate through open ocean than it will in coastal waters. These classifications have also been shown to account for certain general concentrations of chlorophyll from phytoplankton in the water column, which allows for a better prediction of how light will be absorbed or scattered [7]. Jerlov assigned a water type number based on its transmittance of light which was subsequently divided into open ocean and coastal environments. The more heavily a selected amount of radiation was attenuated, the higher the number it was assigned. Therefore, given the Jerlov classification of a body of water, certain attenuation rates based on scattering and absorption can be assumed. The transmittance of wavelengths ranging from 300 nm to 700 nm based on Jerlov classification can be seen below in Figure 4.

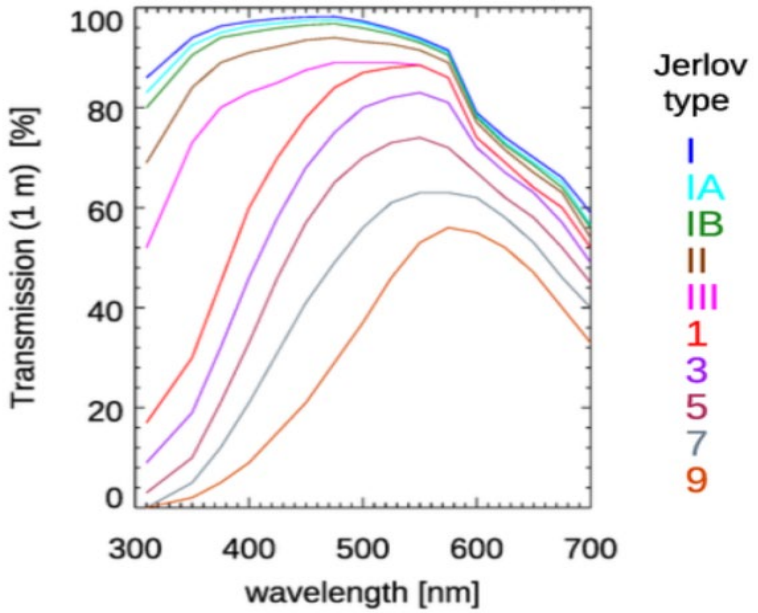

Figure 4. Transmission of radiation based on Jerlov Water Classification. Source: [3]

C. THE UNDERWATER LIDAR EQUATION

The general lidar equation applicable to this thesis is fully derived in [8]. Not only is this equation the backbone of laser navigation using air as a transmission medium, but it is also the progenitor of underwater laser navigation. The equation uses several important assumptions that relate to the proceeding sections. The general lidar equation, also known as the basic scattering lidar equation, consists of several distinct features that relate the emitted energy to the received energy:

$$E(\lambda, R) = E_0\, \xi(\lambda)\, T(R)\, G(R) \frac{A_0}{R^2} \beta(\lambda_L, \lambda, R) \frac{c\tau_0}{2} + BG(\lambda_L)$$

where

- E_0 represents the output energy of the laser pulse.
- $\xi(\lambda)$ represents the receiver's spectral transmission factor to include the influence of any spectrally selecting elements such as a filter at wavelength λ.

- $T(R)$ represents the transmission factor at range R.
- $G(R)$ represents the probability that radiation, scattering from the target at range R, reaches the detector based on geometrical considerations.
- $\frac{A_0}{R^2}$ represents the acceptance solid angle of the receiver optics with area A_0.
- $\beta(\lambda_L, \lambda, R)$ represents the volume backscattering coefficient as a function of the emitted laser wavelength λ_L and the overall wavelength λ at range R.
- c represents the speed of light in the transmission material.
- τ_0 represents the integration time of the detector.
- $BG(\lambda_L)$ represents noise added to the received signal that does not represent a valid return.

1. Laser Output Energy

The general lidar equation is formed such that each term distinctly describes a way for the underwater environment to affect a propagating laser signal. Beginning with the first term, the initial output energy E_0 of a pulse of light is produced by a laser system and emitted through an optical system attached to that laser system. The basics of laser physics will not be described here, although a complete description is provided in [8]. The approximate number of photons in the initial pulse is simply $\frac{E_0}{hf}$, where f is the frequency of the laser light and h is the Planck constant. For this thesis, commercial lidar systems are applied without regard to construction and only evaluated based on the output power provided by these systems; the output power will be assumed constant. This initial energy will only decrease upon propagation within the water column (due to scattering and other loss mechanisms) until it is received by the receiver optics and eventually the detector. This attenuation is described by the following terms in the general lidar equation. In order to maintain the covert nature of light, certain phenomena

involving light, and matter must be avoided, particularly the optical breakdown of certain materials such as water. In [9] and [10], this optical breakdown is described to occur when light of sufficient enough energy interacts with a fluid. This in turn causes a vaporized parcel of liquid to form, cavitate, and create sound. As long as the initial power maintains below this threshold, optical breakdown will not occur, and covert operation can continue. As discussed in [10], laser induced cavitation was tested and observed at a minimum energy of 20 mJ with a 12 ns pulse length, which is nearly twice the amount of energy tested in this thesis. The units for initial output energy are in joules.

2. Spectral Transmission Factor

The second term, denoted by $\xi(\lambda)$, allows for the filtering of incoming light to the receiver. Specifically, this term describes the fraction of light incident on the receiver at a given wavelength that is detected by the detector. However, in certain sections of the water column, the surrounding background radiation from the sun may interfere with the received signal, making the received signal appear larger. This could overwhelm the signal from the lidar system. By adding a monochromator or notch filter, the light can be filtered such that the detector can look strictly for the emitted laser wavelength, negating most of the background sources except where they overlap with the laser wavelength. For this thesis, a filter will be assumed to be installed and calibrated to the chosen laser wavelength that the laser system will operate at, thereby making the spectral transmission factor equal to one for this wavelength. The spectral transmission factor is unitless.

3. Transmission Factor

The third term $T(R)$ describes how the radiation is affected by its propagation through the water column via scattering and absorption interactions by the surrounding water and the other materials it contains. This factor will be assumed to follow the Beer-Lambert law. For simplicity, the wavelength will be assumed constant due to completely elastic interactions and therefore the total attenuation will not depend on the change in wavelength. In more complex environments, fluorescence may occur which would cause the absorbed radiation to shift wavelength. This would change the general lidar equation to another form which is described in [8], only if the resulting wavelength matters to the

receiver. However, for lidar navigation in which a monochromator is used and thus only a certain wavelength will be received, the shifted radiation will be assumed lost, and fluorescence can be considered as a general absorption factor. The transmission factor is provided here:

$$T(R) = e^{-2\int_0^R \varepsilon(R)dR}$$

where $\varepsilon(R)$ represents the total attenuation factor of the output energy as it travels a distance R via both scattering and absorption interactions. This factor is essentially the Beer-Lambert law but differs in that it is only a multiplication factor and also includes a factor of two in the exponent; this extra factor indicates that the law describes the attenuation of the signal in both directions, from the laser source to the seafloor and then back to the detector.

The total attenuation factor incorporates both the scattering and absorption coefficients which are properties of pure ocean water and the material that the ocean water holds within itself. As described in [3], while scattering is very weakly spectrally dependent, absorption is highly spectrally dependent. Therefore, by selecting only a particular wavelength for which the system propagates at, a definite amount of radiation is absorbed and thus the propagation attenuation factor will only be influenced by range and by the concentration of spectrally dependent absorbing materials in the propagation path. The transmission factor is unitless.

4. Geometrical Factor and Receiver Optics Factor

The fourth term $G(R)$ describes how the geometrical design of the receiver optics and laser emitter affect the amount of radiation received at the detector following its travel through the water column. In particular, it represents the fraction of the light received by the detector due to the geometry of the lidar system and the finite size of the system optics. In this thesis, $G(R)$ will take the form of a simple overlap factor as derived in [8], and is represented as:

$$\xi(R) = \frac{A(r_T, W(R), d(R))}{\pi W^2(R)}$$

This equation consists of an area overlap factor (A) that is a function of the target plane radius r_T, the laser beam radius W, and the separation d of the telescope and laser axes in the target plane. The interaction of these terms can be seen in Figure 5.

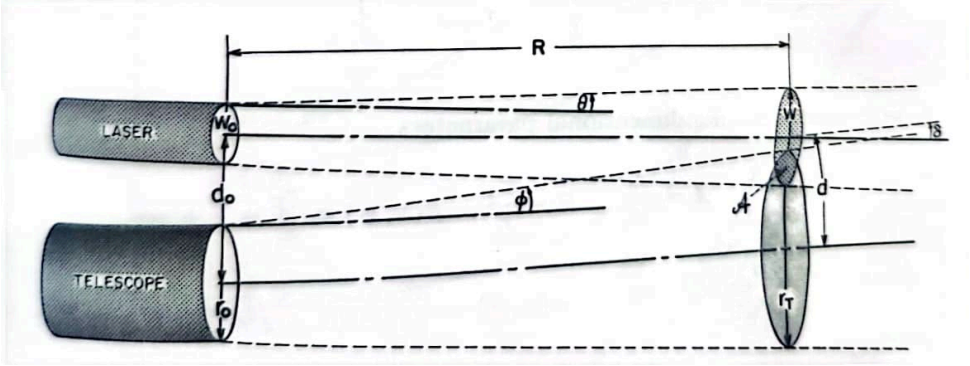

Figure 5. Simple overlap factor. Source: [8]

The target plane radius is the radius of the field of view of the detector at a distance R from the lidar. It is a function of the effective radius of the telescope lens, the range to the target plane, and the receiver-optics half opening angle (which is also a function of the detector radius and the telescope focal length).

The laser beam radius is itself a function of the laser output aperture radius, the range from the emitter to the point in question, and the laser half-divergence angle. The separation distance of the axes is a function of the physical separation between the emitter and the receiver, the range from the system to the target plane, and the inclination angle between the laser and telescope axes. All of these individual equations can be found in the derivation of the simple overlap factor in [8].

Different geometrical designs of the system will affect the overall probability that radiation that is emitted reaches the receiver to be detected. A coaxial design in which the receiver and emitter are on the same axis would produce a probability of detection of one; however, any radiation that is backscattered would be detectable throughout the time of

propagation potentially affecting the perceived depth. By splitting the receiver and emitter into two different axes, depicted pictorially in Figure 5, and having the field of view of the receiver align with the target area illuminated by the emitter, much of the initial backscattered light can be mitigated. This will allow for a return signal that experiences a reduced amount of noise and detection error at the expense of increased system complexity.

This particular geometrical design can be seen modeled in Figure 6. In this figure, only the portion of the laser beam that falls within the detector FOV will be counted towards the detection probability. Notice the segment of the laser that falls outside of the FOV (i.e., depths less than 30 feet); this portion, and any backscatter produced by it, will not count as a return from the detector. In Figure 7, the effect of the example configuration shown in Figure 6 is shown. Notice how as the depth increases, and more of the laser beam is encompassed into the receiver FOV, the value of the simple overlap factor increases.

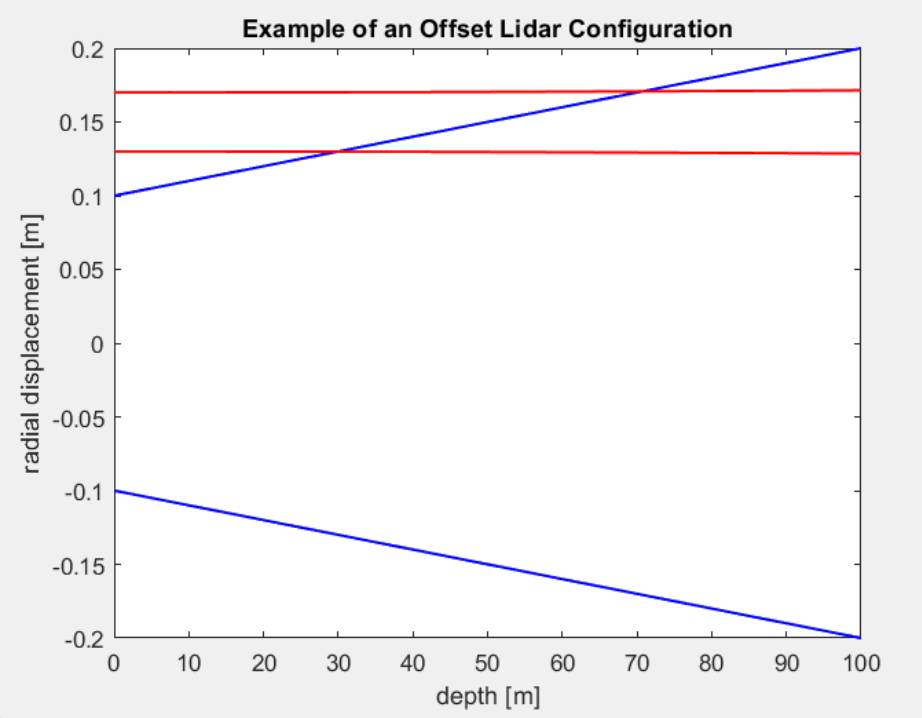

Figure 6. Example of an offset lidar configuration, red indicates laser diameter, blue indicates acceptance range of detector.

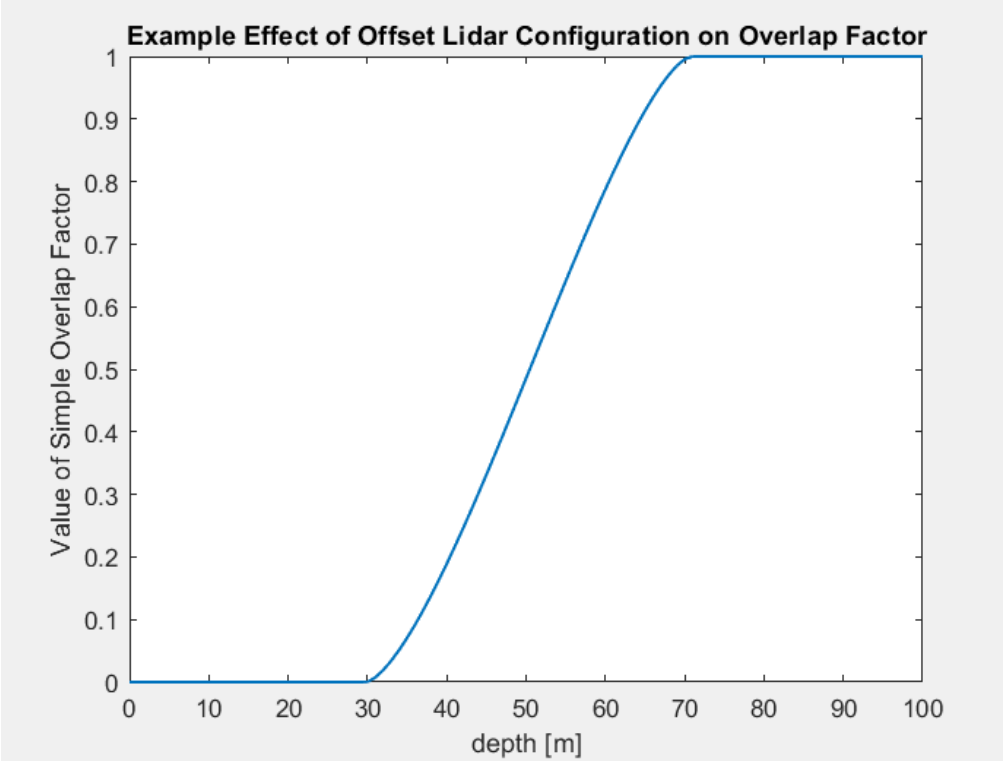

Figure 7. Results of simple overlap factor changing with depth in an example system configuration.

The fifth term of the general lidar equation, the receiver optics factor $\frac{A_0}{R^2}$, describes the field of view of the receiver in terms of solid angles. Any light that is reflected by the illuminated target area must land within the receiver field of view in order to be detected.

For both of these factors, the laser pulse distribution is assumed to be Gaussian, and the temporal profile of the pulse is assumed to be rectangular in shape, which is comparable to most commercial lidar systems. The separation distance and angle of the emitter both affect the system. These factors are used to develop the program used in this thesis to calculate the geometric form factor for a given setup. The geometrical form factor is unitless, but the receiver optics factor is measured in inverse meters.

5. Backscattering Coefficient

The sixth term $\beta(\lambda_L, \lambda, R)$ describes the ability and direction of the water column and the material held within it to scatter the incoming radiation back toward the detector.

The backscatter coefficient is a factor provided by the angular distribution of scattered energy at a particular scattering angle [3]. Additionally, the backscattering coefficient is the component that represents backscatter within the total extinction coefficient in the Beer-Lambert law. Typically, radiation will be weighted heavily to continue propagating in its direction of travel; thus, angles that are close to the original path direction will have higher values of β to indicate that the majority of radiation will continue in the forward direction. However, as radiation is scattered by water molecules and other detritus in the water column, some of the incoming radiation will be scattered in different directions based on the properties of the scattering material. Most scattering angles will not be of significant importance as they will only contribute to the total attenuation of the incoming radiation. Backscatter — the range of angles closest to the 180-degree scattering angle — can provide a significant amount of noise at the detector and thus are more important in lidar navigation. The backscattering coefficient is measured in inverse meters.

The seafloor reflectivity measures the level of backscatter of the seafloor, typically understood as a percentage of light that is reflected back towards the detector. Since the seafloor is not perfectly smooth, and in most cases is very rough, these reflectivities are small. The seafloor is therefore considered a Lambertian (or diffuse) reflector, which means that it reflects light diffusely and only a small amount of light is directed along the original axis. This term is included within the overall backscatter coefficient as a multiplication factor but not as a separate term in the general lidar equation. The seafloor reflectivity coefficient is unitless and is represented as a percentage. The reflectivity acts like backscatter at the depth where the light interfaces with the seafloor and will be considered so in the model. Overall, the relationship will be defined by [3]:

$$\beta \frac{c\tau_0}{2} = \frac{r}{\pi}$$

where r is the reflectivity of the seafloor.

6. Detector Operation Factor

The seventh term $\frac{c\tau_0}{2}$ describes the time that a detector will be active to receive any returning radiation. The integration time τ_0 is of particular importance as it affects the return signal. Increasing the integration time would allow for more energy to be received at the detector from all sources, the most prevalent being backscatter, which is not wanted. As a drawback, the increase in the amount of backscattered light (noise) that is received by the detector could ultimately raise the noise floor above the signal level. If this occurred, the seafloor would not be detected. In order to increase the reliability of a detection of the seafloor the integration time must be reduced until its magnitude equals that of the laser pulse length; this allows only the laser pulse to be received and the remaining backscattered light to be omitted.

7. Background Radiation Power

The final term in the general lidar equation is the noise that is at the laser wavelength, accounted for by the term $BG(\lambda_L)$. This could either be to noise inherent in the detector or due to scattering from sources other than the lidar laser source. Increasing this power would increase the overall strength of the received signal, but since this power derives from sources other than the laser beam, its existence detracts from the overall accuracy of the system. To reduce this factor: add filters, move to a lower depth, and improve the system design to minimize electronic noise. The background radiation factor is measured in joules.

THIS PAGE INTENTIONALLY LEFT BLANK

III. DATABASES AND METHODOLOGY

The general lidar equation, supplemented by the Beer-Lambert Law, is accurate enough to build a sufficient estimate of lidar performance underwater. The model describes the attenuation processes that exist underwater and allows a reasonable estimate of the return signal from a diffuse reflection representing scattering from the seafloor. This could be useful for the safety and navigation of an underwater vehicle. However, before describing the full methodology of the model in subsequent sections, a background in the database used by the model must be provided. This chapter will also provide the underlying assumptions that dictate the modeling and results that are described in the next chapter.

A. NAVAL INFORMATION WARFARE CENTER DATA

The Naval Information Warfare Center (NIWC) [11] provided sample data from optical experiments in water off of the coast of California. Three particular datasets were included, each taken during a different time of year to evaluate the optical properties of water during different seasons, specifically Fall, Spring, and Summer. Both the Fall and Spring datasets were sampled to the same depth, allowing for consistent testing between the two. The summer dataset was limited to a much shallower depth for unknown reasons, which limited its effectiveness in testing the lidar model as compared to the other two datasets. The water column was sampled by lowering an optical measuring apparatus into the ocean. The apparatus would then shine laser light through a small sample of ocean water and measure the amount of light that was backscattered and attenuated. Meanwhile a separate detector on the apparatus measured the ambient sunlight reaching the detector. The specific data used in this thesis, from all datasets, included both the measure of attenuation and the measure of the level of light backscatter throughout the entire water column. Data that was not actively used in the model, but was provided, included the level of photosynthetically available radiation (PAR). This particular piece of data provided insight on the depth and strength of the euphotic zone, as this type of radiation is what photosynthetic materials use to generate photosynthesis.

Additionally, temperature data was also provided which allowed for a deeper understanding of the relationship between optical properties and water temperature. These two parameters were not used in the simulation directly and any effect that the parameters have on the propagation of light would be accounted for within the lidar equation.

B. WORLDWIDE OCEAN OPTICS DATABASE

The Worldwide Ocean Optics Database (WOOD) [12] provides every optical factor that is relevant to underwater laser propagation, as described in the lidar equation. Additionally, it provides many other factors that could further improve any model based upon it. The database provides these factors which are taken from select locations across the Earth's oceans and provides a convenient way to access any optical factor needed. The database contains vertical profiles of these select locations to provide data for optical properties, nutrients, chlorophyll, temperature, salinity, water depth, etc. Unlike databases provided by NASA or NOAA, which are either held behind secure systems or are difficult to easily traverse, the WOOD stores data in publicly accessible files in a text format that is easily manipulated in Microsoft Excel or MATLAB. Specific water locations are then accessed by latitude and longitude, and then by the requested data. The data is collected in a similar manner to the NIWC data: by lowering a detector into the water column and collecting the specific data at each depth. The data is based on a specific wavelength of light (primarily 490 nm); however, this data, along with the background information discussed in Chapter II, is useful to derive close enough estimations of actual values based on water properties and the equations that govern the results at any wavelength.

C. METHODOLOGY

In order to fully explore the optical data provided by NIWC and WOOD, and to validate the feasibility of using lidar signals underwater, a MATLAB model was derived from the general lidar equation. This model based its attenuation on the Beer-Lambert law and does not include any complex effects like fluorescence, multi-scattering events, or Raman scattering. While submarine navigation and safety require some level of

accuracy, including these complex effects would have overly complicated the model and would have added only a slightly higher level of accuracy. With a larger amount of added computation time, complexity of this level was not necessary for this purpose.

Two MATLAB scripts were created to import the relevant optical data from both NIWC and WOOD. Each database required a separate script to manage the data, as neither database followed a standardized data presentation convention. Additionally, the script that processed the WOOD data plotted the provided latitude and longitude to create a map of data collection points. This map was used to locate areas that had a high concentration of data. The generated map clearly showed that data had not been collected everywhere and thus the data cannot be considered all-encompassing for every water type. However, several notable locations were included such as both coasts of the United States, the East and South China Seas, portions of the Arctic, and the Mediterranean Sea. All of these areas are important to operations of underwater vehicles, but the East China Sea and Sea of Japan were the only data that were used. The choice of locations was arbitrary. These data processing scripts, as well as the general lidar calculation script, are provided in the appendices. The map of the locations used that was generated by this script is provided as Figure 8.

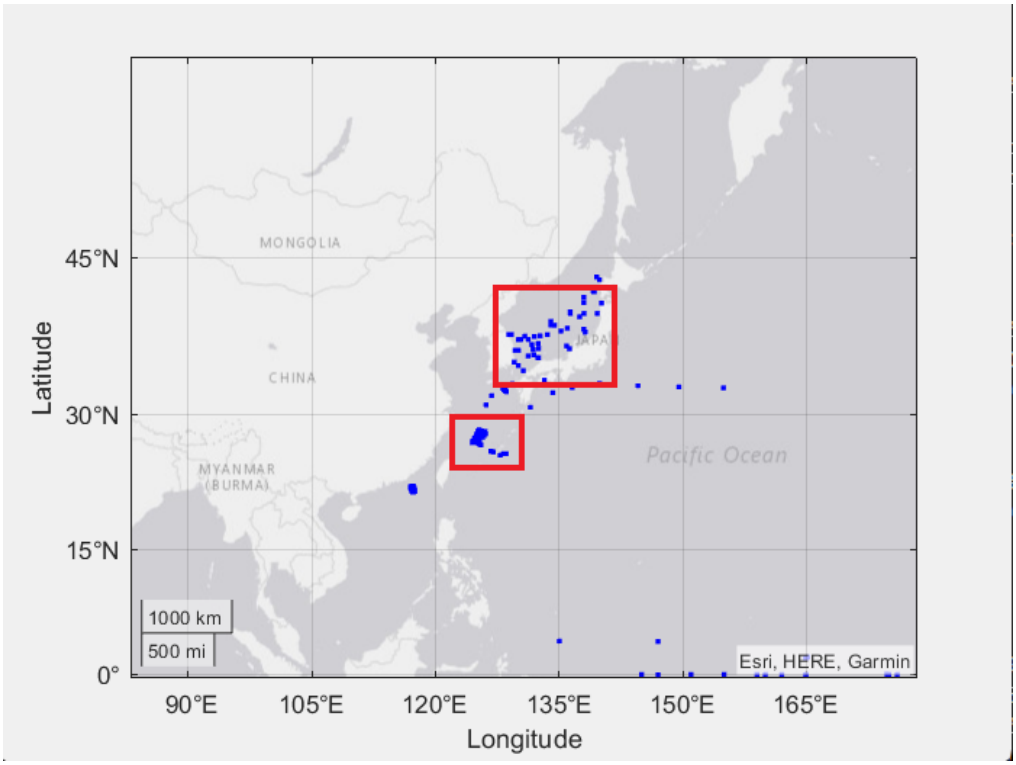

Figure 8. Map of data locations used by the worldwide ocean optics database (WOOD).

Once the data was converted into a usable data file and the location of interest was selected, the data was gathered and used within several individual scripts that calculate the received photon count at the detector based upon the general lidar equation described in Chapter II. An additional script was also included to graphically display the overlap factor used in the lidar equation. While not directly necessary for the results of seafloor depth detection, this plotted geometry was useful in conceptualizing the amount of backscatter that could be present in the return signal based on the geometry between the emitter and detector. Several wavelengths were tested using the reference data provided by WOOD; these wavelengths were selected as close to 532 nm as the dataset allowed, because this particular wavelength is a commonly available commercial laser wavelength. Wavelengths near 532 nm also correspond to a minimum of attenuation.

Once the data was gathered and organized, the model was able to be used. Several inputs were needed in order to run the code, all of which were either taken from

commercial laser capabilities or, if they were not found on commercial specification sheets, were assumed to be conservative values based on the lidar equation and physics. These inputs are described in Table 1.

Table 1. Input values for general lidar equation model

Peak Laser Power, P_0	1 MW
Laser Pulse Length, τ	1 ns
Integration Time, τ_0	1 ns
Laser Beam Waist, W_0	0.05 m
Laser Beam Quality, M^2	1
Laser Wavelength, λ	470 nm
Detector Radius, $r_{detector}$	1 mm
Telescope Radius, $r_{telescope}$	10 cm
Emitter/Sensor Separation Distance	0 m
Telescope Focal Length	1 m
Inclination Angle, δ	0°
Background Power, P_{BG}	0 W

First was the desired peak output power of the laser, which was selected to be 1 MW. This power can easily be reached by commercial and military lasers by using pulses of sufficiently short length, while maintaining a reasonable average power output. The pulse length time was therefore selected to be 1 ns, which is again achievable by commercial and military lasers. These lasers would therefore emit a signal with an energy of 1 mJ at a minimum. As discussed in Chapter II, the integration time is set equal to the laser pulse length. The laser beam waist was selected to be 0.05 m and the M^2 factor, which measures the quality of the laser beam, was selected to be one. This is the best achievable magnitude for this factor as it can only go up in value and it cannot have a value less than one. These factors are easily achievable by commercially available lasers and when adjusted can increase or decrease the accuracy and range of the system. A detector radius of 1 mm and a telescope radius of 10 cm were selected to mimic commercial lidar systems. The telescope and laser emitter were selected to be coaxial - a separation distance of 0 m - to ensure full detection of the signal, however it should be noted that backscatter will decrease as the emitter and telescope are separated. This is

different from the geometry discussed in the previous chapter. Separating the emitter and telescope too far will drastically reduce the return signal power, however. The telescope focal length was selected to be one meter to assist with the simple geometrical overlap. The inclination angle between the axes of the emitter and detector was set to zero since they are coaxial. However, this number would need to be adjusted if a non-coaxial case were to be tested. Finally, the background power was zeroed in order to look only at the maximum depths achievable by the system. Increasing the background power would further increase realism in future simulations. Seafloor reflectivities were also varied to test the feasibility at any seafloor type and their selection is discussed in Chapter IV.

After the input parameters were added to the code, the MATLAB script would prompt the user to select either the NIWC or WOOD dataset. Selecting one dataset over the other would cause the model to process the data differently in order to gain different results and insights. The NIWC data was used at a set vehicle depth and safety standoff from the seafloor and then the program would run according to what is seen in Figure 9. This would show the technical limitations of the lidar platform, as a specific number of photons were needed at the receiver to detect the seafloor. The minimum sensitivity selected for the detector was a detection threshold of 10^4-10^5 photons, above background and per pulse, captured by the detector from light reflecting from the seafloor, which allowed for a sufficiently distinct return peak that is easily distinguished from environmental and system noise [13]. Therefore, if the model received a return signal that was 10^4-10^5 photons or greater, it was considered a positive return. If the return was less than 10^4 photons, it would not be considered a successful detection of the seafloor. The seafloor was also modeled as a Lambertian reflector, which means it scatters light diffusely. As the light from the emitter interacts with the seafloor, roughness from the sediment causes light to be scattered in all directions as well as reflected back to the vehicle. Since the seafloor varies drastically at any point on the earth, a range of seafloor reflectivities (from 10-70%) was used to fully cover this variability. The depth was then calculated from the total flight time, and the final result was recorded.

The WOOD data used the same input parameters but did not account for a safety standoff distance. For this data and the NIWC data, the seafloor reflectivities were

iterated over and the vehicle depth was changed in each iteration over which the water column was sampled. In each iteration, the model would calculate the photon count at the vehicle depth and then move the seafloor lower until the seafloor was at the final depth included in the dataset, sampling at each depth. This photon count data was then recorded and would be compared against the minimum sensitivity of the detector. If the photon count was greater than 10^4 photons, the depth would be recorded as a detection. If not, no depth was recorded, and the vehicle was moved to a new depth. Finally, the difference between the maximum detected depth and the vehicle depth was taken in order to show how far below the vehicle keel the system could detect the seafloor.

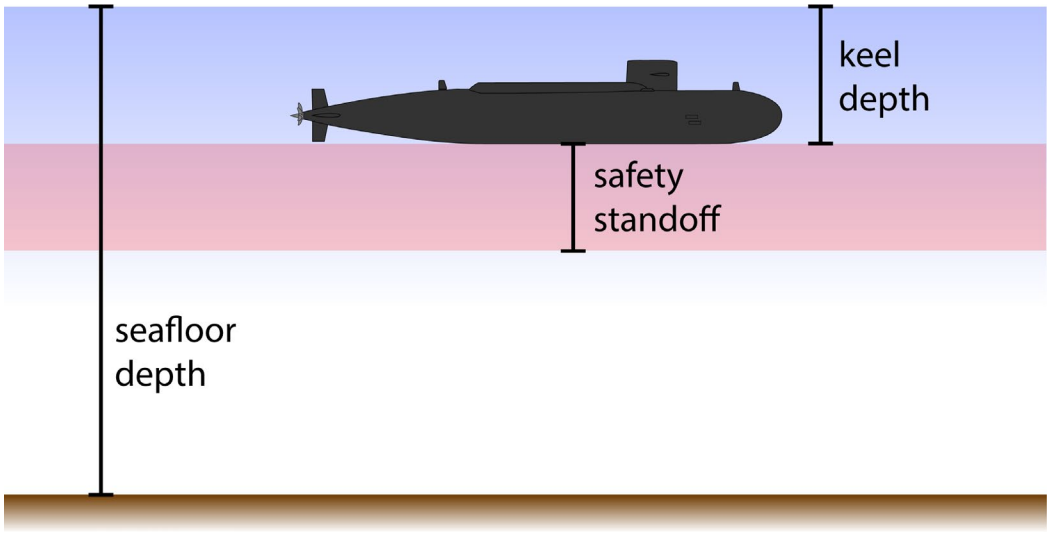

Figure 9. Geometry of the simulations in the MATLAB script.

There was one significant issue with the WOOD database: the two parameters that were used in the lidar model, the attenuation coefficient and backscatter coefficient, were not observed at the same time or location. The test points for the attenuation coefficient sometimes aligned with that of the backscatter data locations, but even in the small number of cases where that was true, the data was taken years apart. However, the assumption was made that the backscatter and attenuation data were taken in the same relative area and did not differ much over time; therefore, it was assumed that they could be used together to describe the water optical quality accurately. The main vertical

structural components of the water column were maintained throughout several years and differed very slightly in magnitude, which was the justification used for this assumption.

Another issue was that the data points were not taken at a consistent wavelength. The data was spread across several wavelengths, which could drastically affect the resultant power received at the receiver, based on prior discussions of absorption and scattering. The assumption was made in this model that the absorption and scattering properties of pure seawater and the organic and inorganic material contained within it are roughly the same over a range of wavelengths from 440 nm to 570 nm. While this is not necessarily true for most optical properties, without this assumption the database would have only been able to provide one or two overall results, which is insufficient to be able to evaluate the feasibility of lidar. This is an assumption that could be fixed in the future by sampling all of the optical properties at the same time, like for the NIWC dataset.

IV. MODELING RESULTS

The general lidar equation model produced results that confirm the hypothesis that a pulsed laser system would be able to provide enough data returning to the detector to keep an underwater vehicle safe. This result depends on the safety standoff distance required by the mission, which was specified in the model's initial parameters. Additionally, the depths that were detected by this model could provide accurate navigational insight for vehicles that want to operate in water that is deeper than the shallowest of coastal waters. The model did need several assumptions that are not entirely realistic, however, and the results provided by a deployed lidar system may differ significantly from the results of this model.

A. RESULTS USING NIWC DATA

Utilizing the NIWC data seemed to provide the most enlightening results with the least number of assumptions. The data provided by NIWC (which was collected off of the coast of California) was separated into the different seasons in which the data was collected. Attenuation and backscatter data were collected in fall, spring, and summer. There was no data collected in winter.

1. Fall. Vehicle at 20, 80 m. Safety Standoff Range at 10 m and 30 m.

In the following figures, based on data taken in the fall, the vehicle depth is first selected to be 20 m, which is in the high attenuation region of the euphotic zone, and then selected at 80 m, which is well below the high attenuation region. Both of these depths are reasonable for underwater vehicle operations. The euphotic zone can extend several hundred meters into the water column, but for this thesis the high attenuation region was the most important to consider. This region in particular was considered interchangeable with the euphotic zone as a whole.

Figure 10 is created directly from raw data provided by NIWC, with the attenuation plotted as a function of depth below the ocean surface. The euphotic zone is characterized by a substantial increase in attenuation, reaching a maximum of

approximately 0.275 m^{-1} at a depth of approximately 30 m. This attenuation data was used along with provided backscatter coefficient data as inputs to the general lidar equation model. For this case, the bottom of the vehicle was located at a depth of 20 m, which can be seen to be above the depth for maximum attenuation.

Figure 11 shows results from the lidar equation model, using NIWC data taken in the fall. Specifically, this figure shows the total number of photons received (horizontal axis) by the lidar system as a function of the seafloor depth (vertical axis). In the figure, the labeled horizontal dashed grey lines indicate the keel depth (bottom) of the underwater vehicle and the minimum allowed seafloor depth based on the allowed safety standoff. The safety standoff is based on some arbitrary mission parameter and restricts how close the underwater vehicle can be to the seafloor. If the mission only allowed for the underwater vehicle to come within ten meters of the seafloor, as is the case in this test, then the received photon count for the minimum seafloor depth would be the maximum value expected for that distance. If the seafloor was closer than this distance, then the vehicle would need to take action to maintain its safety.

Figure 11 also shows that at the most limiting seafloor reflectivity (R = 0.1) the deepest seafloor that could be detected is located at ~55 m, which is 35 m below the keel depth of the vehicle. With the most reflective seafloor type (R = 0.7), the seafloor detection was increased to a depth of ~65 m, an overall increase of 10 m in seafloor detection. These depths are entirely reasonable to maintain vehicle safety, depending on the safety standards of the mission.

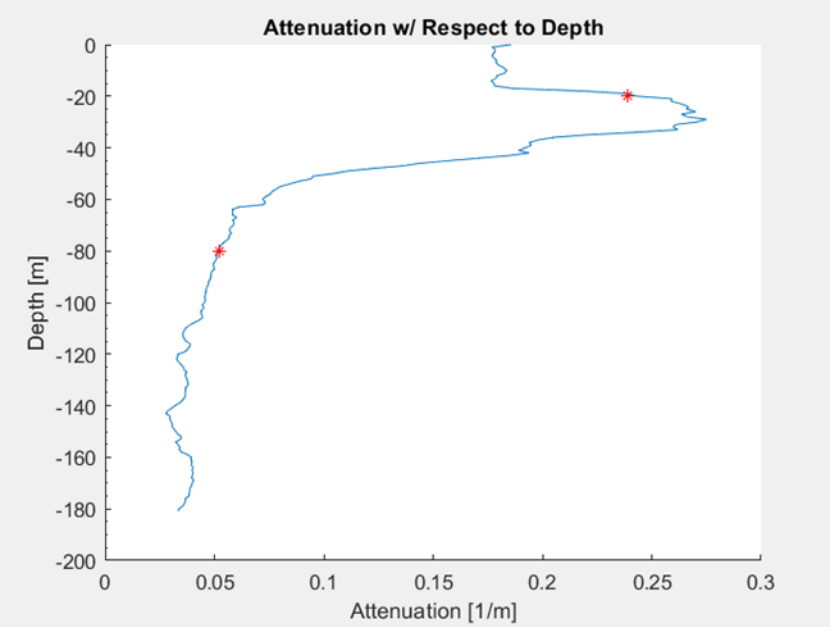

Figure 10. NIWC fall data: attenuation vs. depth, wavelength: 470nm. Vehicle depths of 20 m and 80 m indicated by asterisks.

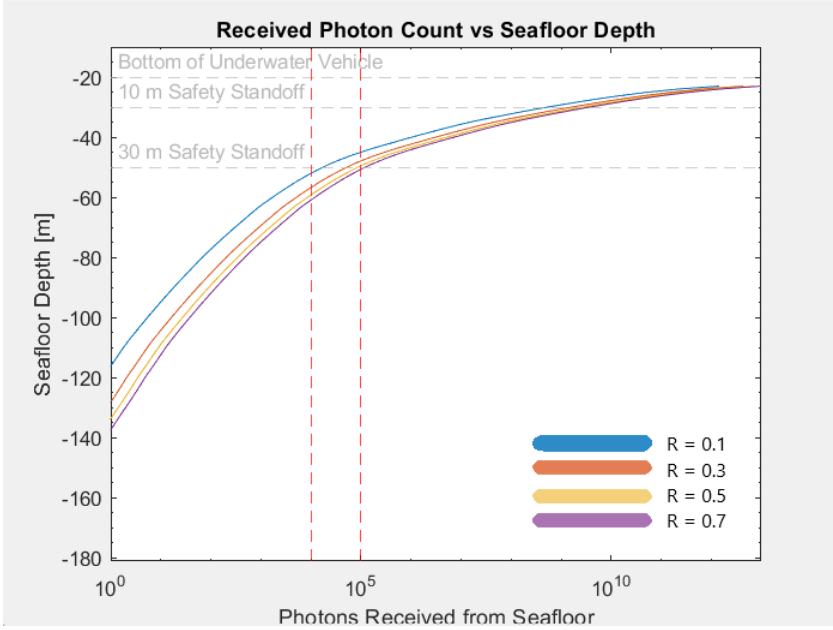

Figure 11. Received photon count vs. seafloor depth, using NIWC fall data. Vehicle depth at 20 m, safety standoff range is 10 m and 30 m.

The colored lines indicate photon counts from signals that interact with different reflective coefficients of the seafloor. From left to right, each line indicates an increased

reflective coefficient, starting from R = 0.1 (10%) on the left and ending at R = 0.7 (70%) on the right, in intervals of 20%. As R increases, these values indicate a more optically reflective seafloor and thus less loss when the lidar signal interacts with the seafloor. As can be seen in Figure 11, the reflective coefficients change the maximum detectable seafloor depth by approximately 10 m from the least to most reflective seafloor types.

The vertical dashed red lines indicate the minimum band of photon count detection that would allow the system to recognize a return in the presence of noise. The leftmost line is at a value of 104 photons and the rightmost line is at a value of 105 photons. These values were chosen based on lidar industry standards for detection [13]. If the magnitude of the received photon count is within or to the right of the area encompassed by the two red lines, the signal will be recognized as a seafloor detection. If any result occurs to the left of the area encompassed by the red lines, then the signal will not be assumed to be detectable.

To show the advantage of operating below the euphotic zone, where the attenuation is significantly lower, Figure 12 shows the received photon count for a vehicle depth of 80 m with the same safety standoff ranges and attenuation profile. The results in Figure 12 show that any seafloor depth below the underwater vehicle stationed at 80 m, until the maximum total water depth sampled in this dataset, will be detected regardless of the seafloor reflectivity coefficient. It could be assumed that if the attenuation parameters at this point were maintained at the same level throughout the rest of the water column, the detectable depth of the seafloor could be much deeper. The most limiting seafloor reflectivity comes close to the band of minimum detector sensitivity; however, this occurs at a depth nearly 100 m below the keel of the vehicle.

Figure 13 shows the relationship between the maximum depth below the keel that a vehicle can detect the seafloor and the depth at which the vehicle emits a laser pulse. Particularly it can be seen that as a vehicle gets lower in the water column the maximum seafloor depth that is sensed increases. This is due to the vehicle passing through the high attenuation region of the euphotic zone. The maximum seafloor depth that can be sensed above the high attenuation region is therefore much less, as the outgoing laser pulse and the return signal from the seafloor both need to propagate through the region where their

overall intensity decreases dramatically. The figure is cutoff in vehicle depth due to artifacts being generated in the low reflectivity case after the depth below keel reaches the maximum depth in the dataset. All reflectivity cases level out along a horizontal asymptote, therefore, the final depth below keel shown on the plot can be extrapolated to any deeper vehicle depth and is maintained at the same value.

Finally, to show the effect of a change in safety standoff range, Figures 11 and 12 also show the results of the received photon count for a vehicle at 20 m and 80 m depth, respectively, with an increased safety standoff range of 30 m. The increased safety standoff range does not affect the overall maximum depth that the lidar system can detect but does reduce the expected received signal if the seafloor were at the standoff range.

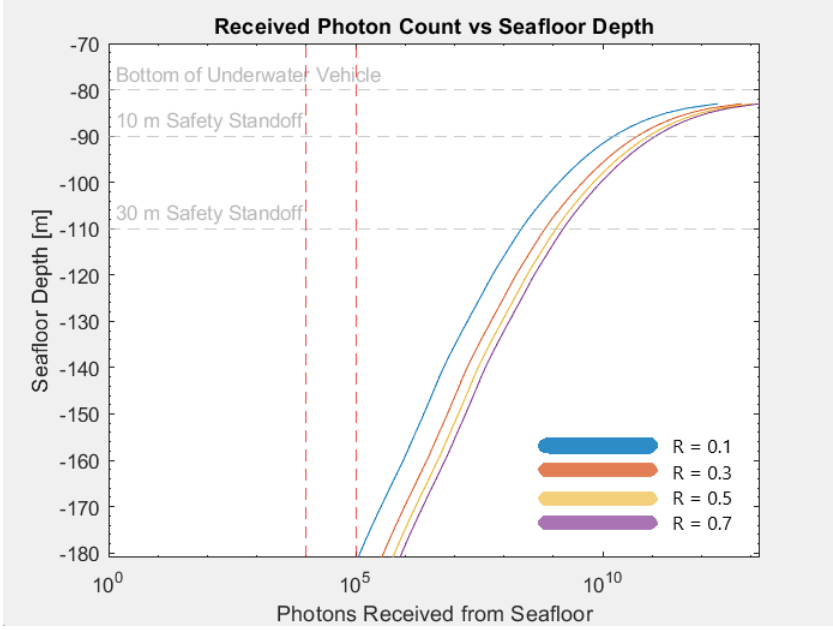

Figure 12. Received photon count vs. seafloor depth, using NIWC fall data. Vehicle depth at 80 m, safety standoff range is 10 m and 30 m.

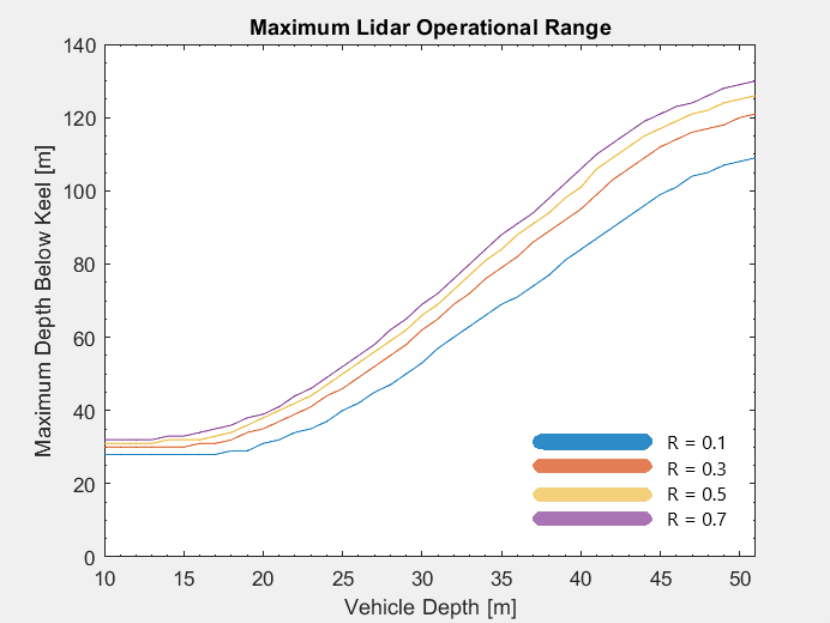

Figure 13. Maximum detectable depth below keel vs. vehicle depth, using NIWC fall data.

2. Spring. Vehicle at 20, 80 m. Safety Standoff Range at 10 m and 30 m.

At the location that the NIWC dataset was recorded, the seasons drastically change the overall attenuation curves and, therefore, the detectable seafloor depth for a lidar system. Figures 14–17 show the attenuation profile and corresponding model results for an underwater vehicle placed in the euphotic zone, as well as below it, during spring. There are notable differences in maximum detected seafloor depths compared with the fall case for the previous plots. The four grouped lines again show the effect of different seafloor reflectivity coefficients, and the red lines again indicate the minimum photon count assumed to be required for detection. The vehicle depth in the euphotic zone was maintained at 20 m. The vehicle depth below the euphotic zone was also held at 80 m to look at attenuation effects outside of the euphotic zone. No other changes to variables in the model were made.

The large seasonal change in magnitude of the attenuation coefficient shows the overall effect it has on the propagation depth of an emitted lidar signal. For example, a vehicle operating at a depth of 20 m within the euphotic zone in the fall can detect the most reflective seafloor ($R = 0.7$) at a depth of approximately 40 m below the keel. The

same type of vehicle during the spring, in the same location with the same seafloor type, would detect the seafloor at a depth of approximately 25 m below the keel.

While lowering the vehicle below the euphotic zone increases seafloor detection ranges altogether, comparing the seasons shows a temporal difference in the magnitude of this increase. Once the vehicle is brought below the euphotic zone into an area of lesser attenuation, the detection range decreases in the spring case as compared to the fall case; this is shown in the comparison of Figures 12 and 16. This is due to the fact that the spring attenuation at its minimum is nearly double that of the minimum attenuation in the fall case. An overall loss of approximately 55 m in seafloor detection range is seen in the spring compared to the fall below the euphotic zone. This is reinforced in Figure 17 which describes the maximum depth below keel that a vehicle can detect.

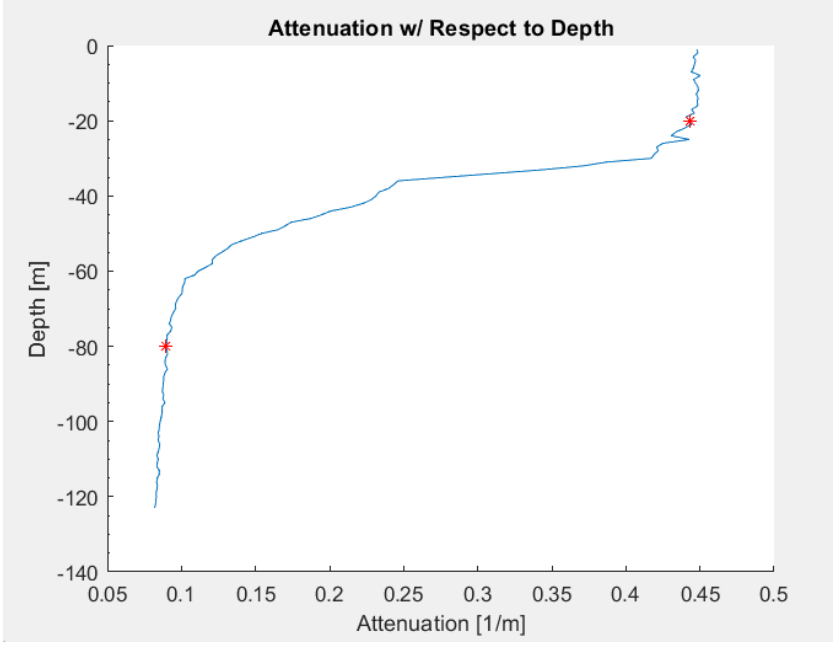

Figure 14. NIWC spring data: attenuation vs. depth, wavelength: 470 nm. Vehicle depths of 20 m and 80 m indicated by asterisks.

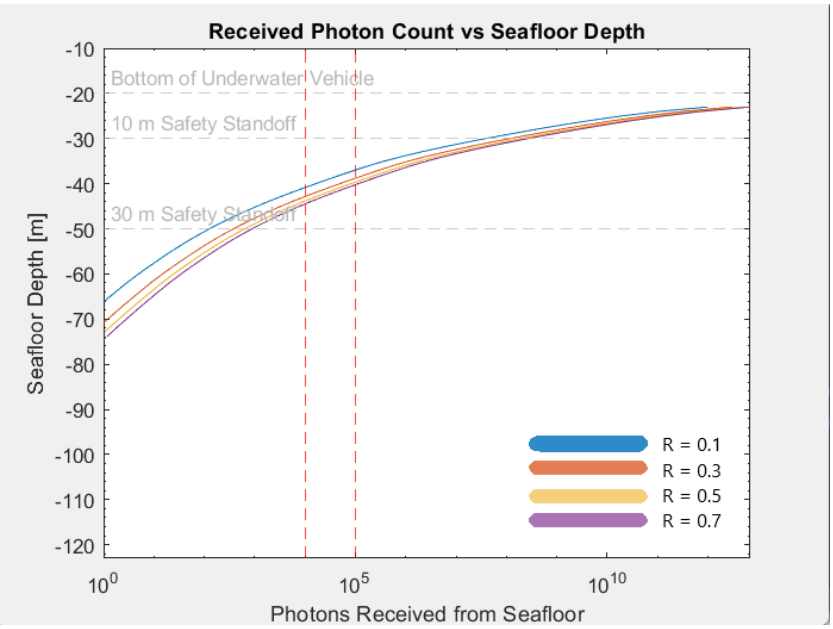

Figure 15. Received photon count vs. seafloor depth, using NIWC spring data. Vehicle depth at 20 m, safety standoff range is 10 m and 30 m.

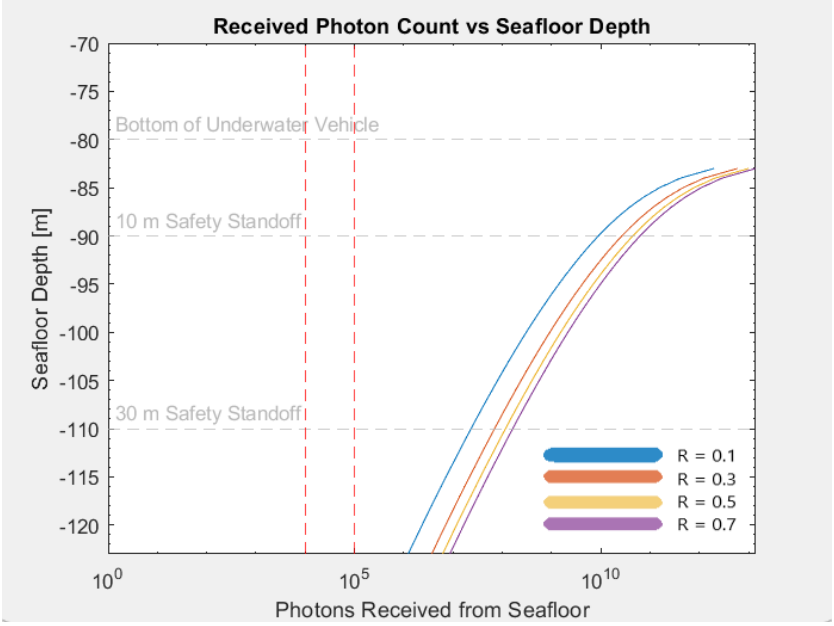

Figure 16. Received photon count vs. seafloor depth, using NIWC spring data. Vehicle depth at 80 m, safety standoff range is 10 m and 30 m.

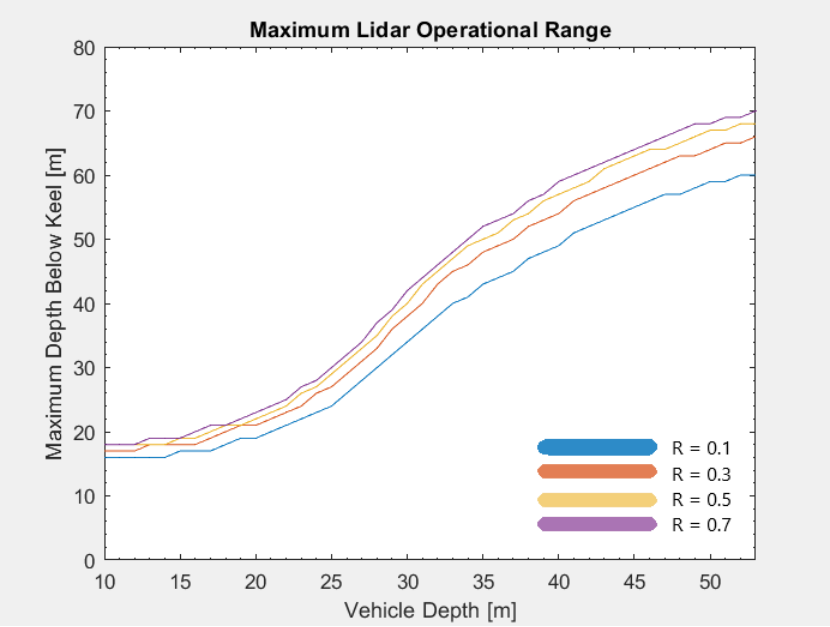

Figure 17. Maximum detectable depth below keel vs. vehicle depth, using NIWC spring data.

Additionally, the importance of an increase in safety standoff range can be seen again in Figures 15 and 16. The results shown in Figure 15 specifically show that in cases of large attenuation, in which the propagation distance is low, an increase in safety range can actually prevent vehicle operation in the location of interest. In this case, if an underwater vehicle is only allowed to be within 30 m of the seafloor and is operating in an area similar to the spring data provided by NIWC, the lidar system will detect the seafloor only within the safety standoff range, with the assumptions made in this model. Since the vehicle would only be able to detect the seafloor within its safety standoff range, it must either leave the area or change its safety standoff range.

The increase in safety standoff range for the case where the vehicle is below the euphotic zone provides the same effect as the fall case did. The overall maximum photon count that a vehicle would expect at the safety standoff range is reduced from the 10 m safety standoff case, but the seafloor remains detectable, as seen in Figure 16.

3. A Note on NIWC Summer Data

The summer data provided by NIWC was also modeled but did not provide any additional information beyond the overall points discussed in the previous sections. Therefore, those figures were not included in this section. However, the figures for the summer, data attenuation and the subsequent results of the model are provided in Appendix A for review.

B. RESULTS USING WOOD DATA

The WOOD database provided detailed information on the optical properties of each location that was sampled. While the assumptions that needed to be made reduced the accuracy and predictive nature of that data, the same trends that were shown in the NIWC data still apply. Therefore, operational data and lidar feasibility can still be evaluated in these locations and treated as if the data was all taken in the same location and time.

1. Sea of Japan

The data presented for the WOOD data is different from the NIWC data and is meant to further highlight the effect that the attenuation curve has on the propagation distance of the lidar signal. To maintain continuity, for all WOOD simulations, the vehicle is set at a specific depth and simulated like the NIWC cases. This specific dataset was gathered from an area in the Sea of Japan. Again, the attenuation curve is provided in Figure 18 and shows the drastic difference of the environment as compared to the NIWC data. Whereas the highest attenuation seen in any of the NIWC data was approximately 0.45 m^{-1}, the attenuation in this data spikes to nearly 1.6 m^{-1} at a depth of approximately 40 m. This attenuation level makes the seafloor nearly impossible to be detected at any depth if the vehicle is positioned above or within this spike. As can be seen in Figure 21, the seafloor cannot be seen in this environment (if the vehicle is above the spike) unless it is within 1 - 20 m of the vehicle keel. This is reinforced in Figure 19, which shows the received photon count for a vehicle positioned above the spike in attenuation. The maximum of this range only occurs if the vehicle is very shallow, and the seafloor is located between it and the maximum attenuation level. Once the vehicle dives below the

spike, however, the detectable range below the keel jumps to approximately 85 m if the reflectivity is high or to approximately 74 m if the reflectivity is low. This is again reinforced by Figure 20, which shows the received photon count of a vehicle positioned at a depth of 80 m.

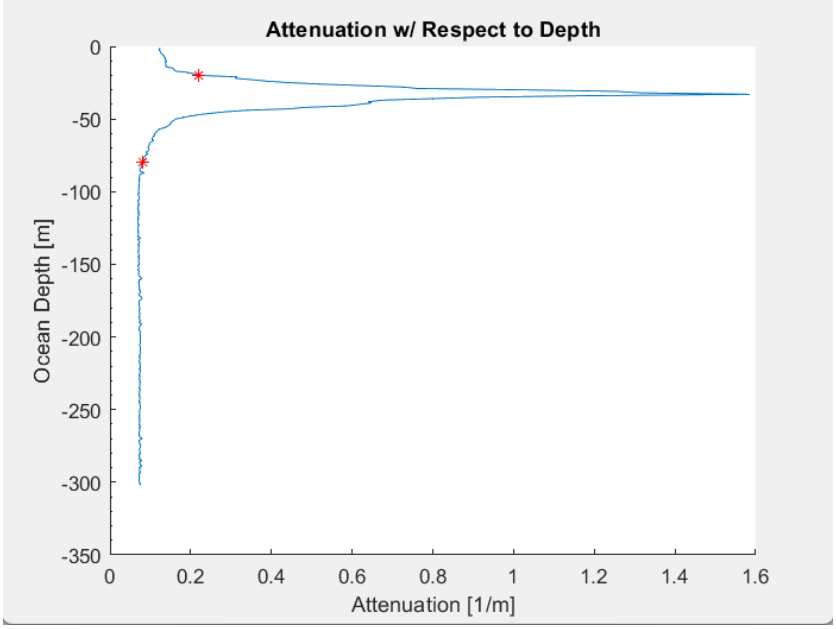

Figure 18. WOOD data, Sea of Japan: attenuation vs. depth

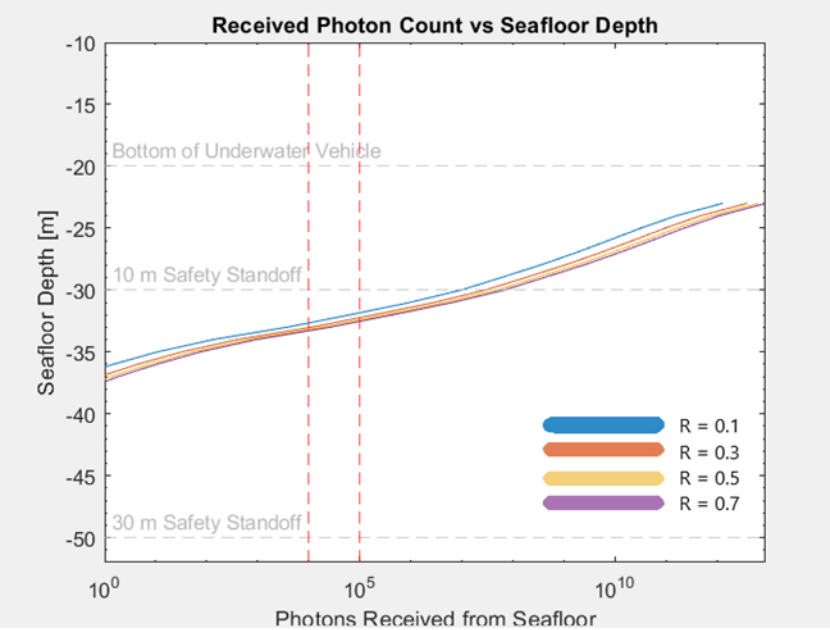

Figure 19. Received photon count vs. seafloor depth, using WOOD data. Sea of Japan. Vehicle depth at 20 m.

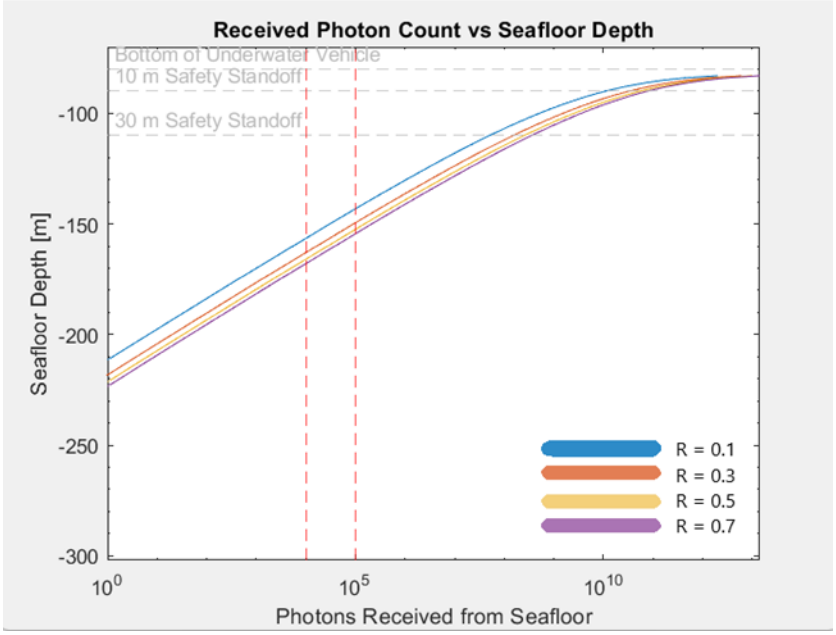

Figure 20. Received photon count vs. seafloor depth, using WOOD data. Sea of Japan. Vehicle depth at 80 m.

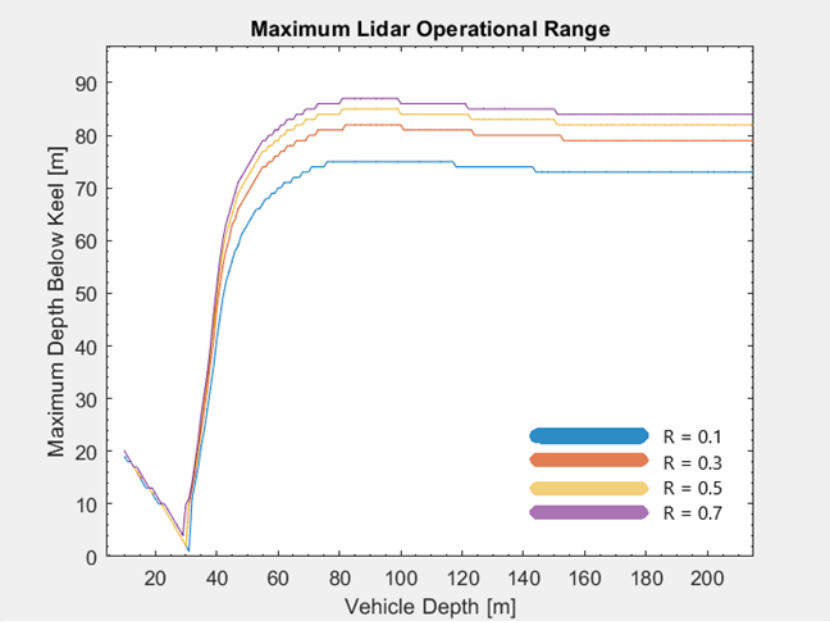

Figure 21. Maximum detectable depth below keel vs. vehicle depth, using WOOD data, Sea of Japan.

2. East China Sea

For data taken in the East China Sea, the attenuation plot looks significantly different from any of the previous tests. This confirms the fact that variability can have drastic effects on performance and a lidar system must be able to operate within the margin of safety set for underwater vehicles in many different, variable areas across the globe. Figure 22 shows the attenuation profile for a general sample area taken within the East China Sea.

Note the large attenuation spike that occurs near the bottom of the sampled data, which is a stark difference from previous tests in which the euphotic zone was much closer to the surface of the water column. Based on multiple sample points within the East China Sea, this is the common type of attenuation profile for this area. This is unlike the Sea of Japan, which had several different attenuation profiles across the samples of the dataset. Another interesting feature of this particular data sample is that it includes two maximums, both of which affect the detectable seafloor depth in similar ways, although the second maximum affects the photon count more than the shallower maximum. Although these both reduce the count more drastically than in depths without

maximums, the overall attenuation is much lower than in the Sea of Japan example, therefore, the lidar signal is able to propagate to the seafloor and return a detectable signal at reasonable depths required for safety and navigation.

Figures 23 and 24 again show the received photon counts based on the depth of the seafloor. It is noteworthy that, in Figure 23, the two maximums seem to be affecting the received photon counts. Having the two maximums in the attenuation profile reduces the maximum depth at which the lidar system can sense. Comparing these figures to Figure 22, however, shows that even though the attenuation profile has two maximums, the magnitude of the attenuation is small enough to not affect the maximum detectable seafloor depth by much. In Figure 24, it is shown that below the first attenuation maximum, no noticeable difference exists between this location and any other discussed previously. Figure 25 again shows the maximum detectable seafloor depth.

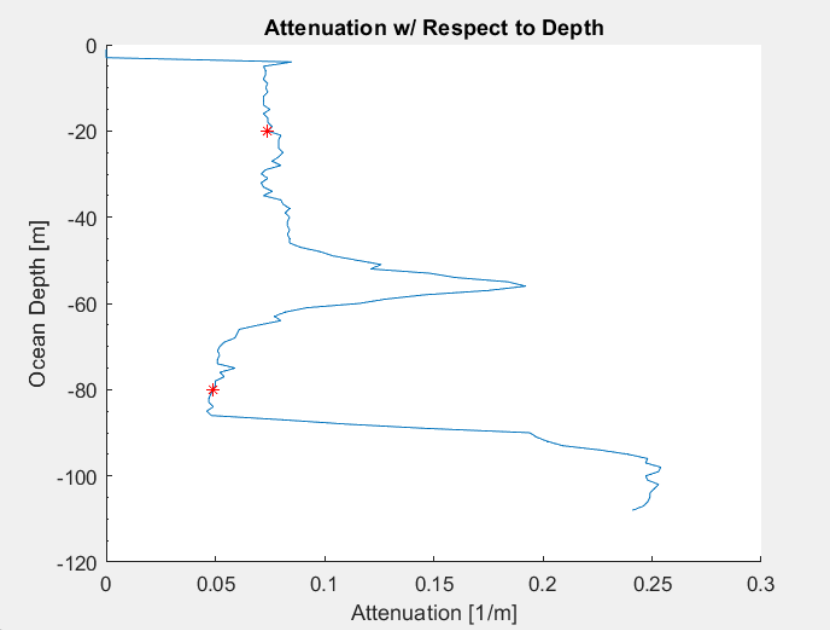

Figure 22. WOOD data, East China Sea: attenuation vs. depth.

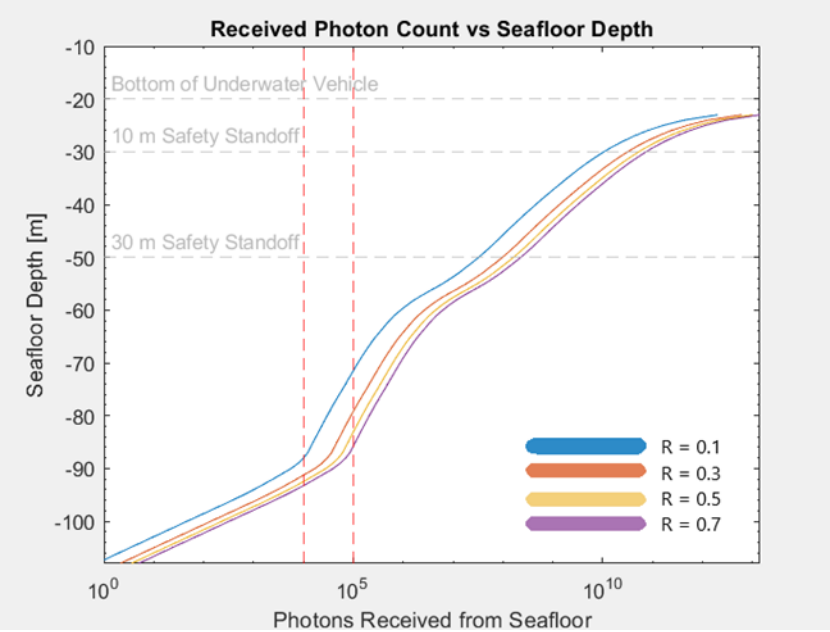

Figure 23. Received photon count vs. seafloor depth, using WOOD data. East China Sea. Vehicle depth at 20 m.

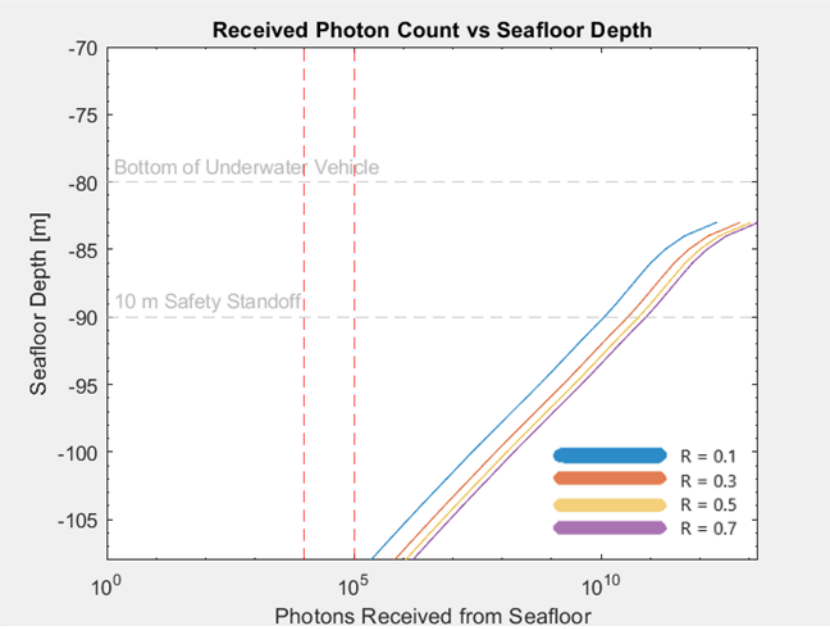

Figure 24. Received photon count vs. seafloor depth, using WOOD data. East China Sea. Vehicle depth at 80 m.

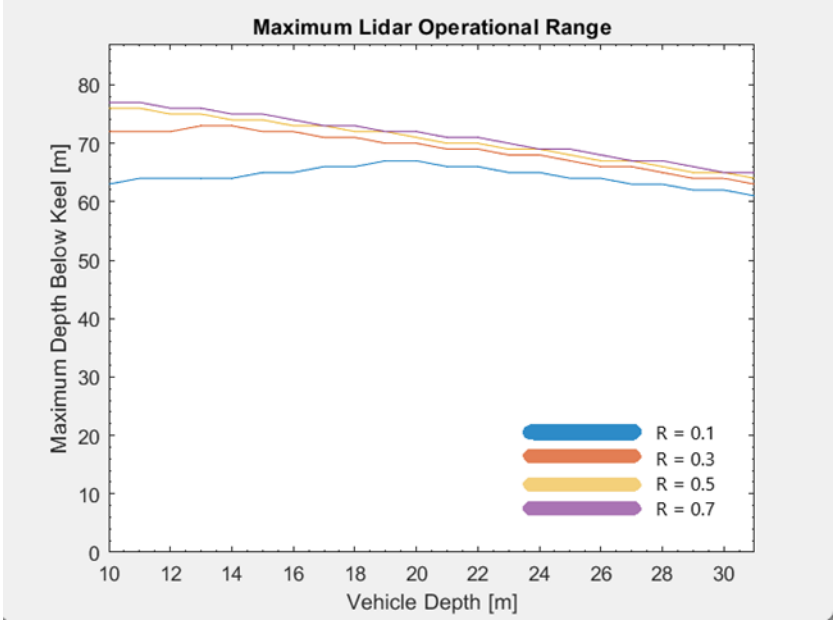

Figure 25. Maximum detectable depth below keel vs. vehicle depth, using WOOD data, East China Sea.

C. A NOTE ON DETECTABILITY OF LIDAR SIGNAL BY ADVERSARIES

Maintaining stealth is a key requirement for underwater vehicles. Whether the vehicle is a submarine or a UUV, maintaining stealth is the most important factor of a mission to ensure the safety of the crew/vehicle and to continue the mission as planned. By implementing a lidar system in place of a normal fathometer in shallow water, the very nature of the optical technology increases the stealth of the vehicle by simply not providing sound energy into the environment, which can be detected fairly easily if an adversary is close enough. An optical system, based on lasers, significantly reduces its detectable signature, as the energy does not spread like sound energy underwater. The majority of the detectable laser energy returning from the seafloor is collimated into a tight beam that would most likely be detected only if an adversarial vehicle is directly above the underwater one. The remaining light would still scatter in all directions, but since it would not get trapped in internal propagation ducts like sound does, the scattering would have to be collected by much more sensitive sensors than described in this thesis. Additionally, the ranges that the adversarial platforms would be likely operating at would be too far to reliably detect the remaining energy scattered into the environment. The

signal would also have to travel through the water column, being attenuated by the Beer-Lambert law the entire time, including the high attenuation region in the euphotic zone. Furthermore, the signal would have to be discriminated from any background light. For all these reasons, detecting these signals would be a difficult task. The only exception would be if detectors were placed in the water column along the path of light before it interacts with the seafloor. This would effectively remove the factor of two in the Beer-Lambert law, drastically increasing its detectability.

In addition to the geometry of the vehicles, many propagation scenarios only allow for the absolute minimum amount of detectable energy to reach the underwater vehicle alone, as shown in the figures in the previous subchapters. The remaining energy that is not captured and is radiated past the underwater vehicle would not be detectable, assuming the adversary is using a similar propagation model and detector. By operating at these specific depths, or by adjusting the output power of the lidar system, the entire system could be tuned in such a way that no detectable light reaches the surface in any scenario. This would make the underwater vehicle completely undetectable, with regard to its bathymetric sensing capabilities, while maintaining the safety of the crew or vehicle by preventing a collision with the seafloor.

THIS PAGE INTENTIONALLY LEFT BLANK

V. CONCLUSION AND FUTURE WORK

Overall, the model created and described in this thesis is effective in manipulating data provided by professional sources to produce meaningful results. Based on the results of the model, after passing NIWC and WOOD data through it, underwater lidar can be used as an alternative to a bathometer in shallow water for the safety of the vehicle. However, the results discussed in this thesis must be understood to be notional, just intended to demonstrate the feasibility of an underwater lidar for this application, based on various assumptions described in the thesis. With the dynamic ocean environment, many variables could drastically change the depths sensed in-situ if a lidar system were to be operated on-board an underwater vehicle. While the system is limited in many scenarios in which the attenuation is high, underwater lidar can propagate far enough to be effective at keeping the underwater vehicle safe. In addition to being able to maintain the safety of the vehicle, the lidar system increases the stealth capabilities of the vehicle by changing the type and reducing the amount of energy output into the environment. While these lidar systems can be large, in general, commercial systems that operate within the parameters used in the model created for this thesis are small enough to add to any underwater vehicle. In conclusion, the lidar system is a completely reasonable technology to use onboard underwater vehicles for safety.

There are several extensions to this thesis that can further prove the system's feasibility as well as increase its capabilities. Firstly, sampling more areas of the ocean for optical data and ensuring all of the data required by this model is taken at the same time will drastically increase the ability of an underwater vehicle to operate in any place around the world. Secondly, evaluating this optical data at a wavelength of 532 nm specifically will ensure that all of the data is useful for an underwater lidar system and ensures the data is selected at the location of minimum attenuation for underwater light propagation. Another extension from this thesis would be to actually validate the model with real data. By comparing the model with data taken in-situ, the overall depths discussed in this thesis could be validated. Finally, extending the use of a laser bathometer, such as the lidar system described in this thesis, in order to perform more

than just a safety role. Several papers exist that could exploit certain physical interactions between light and matter to gain more information on the water column such as water temperature. Also, designing a system that could perform both a safety role and an intelligence gathering role would definitely increase the capabilities of any underwater vehicle equipped with this system. Any of these projects would sufficiently improve the work done in this thesis as well as provide additional features that would improve not only the safety capabilities of this technology, but also increase its capabilities overall.

APPENDIX. NIWC SUMMER DATA

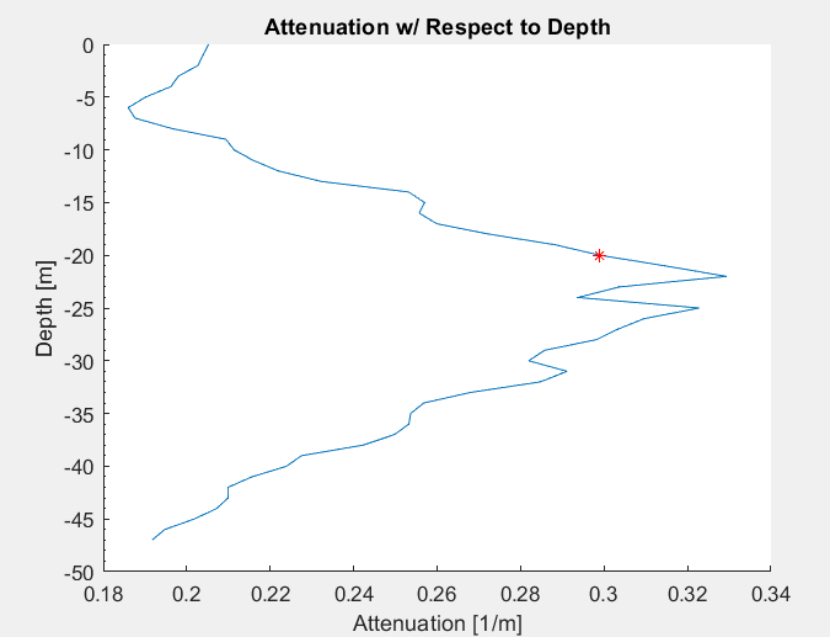

Figure 26. NIWC-provided attenuation data, summer

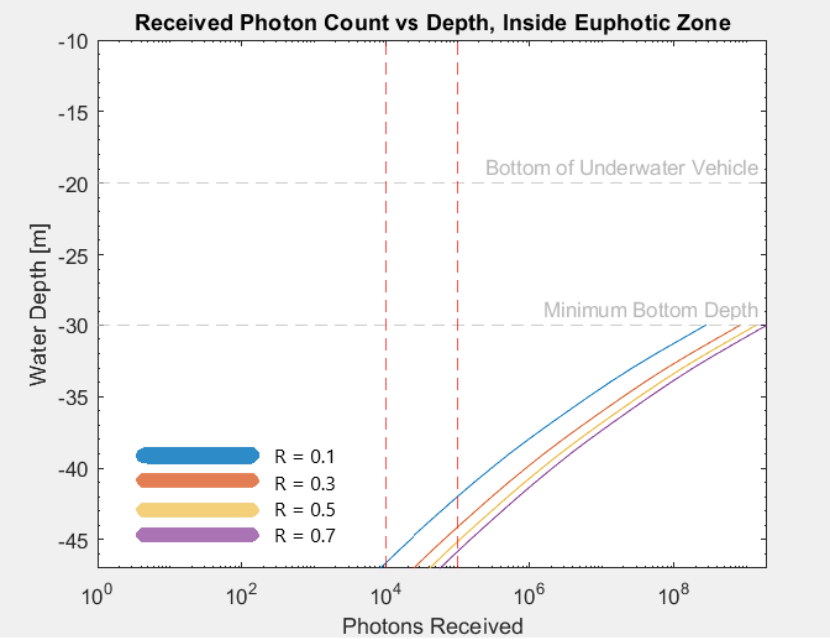

Figure 27. NIWC-provided photon count data, summer

THIS PAGE INTENTIONALLY LEFT BLANK

LIST OF REFERENCES

[1] F. Macomber, "Space Experts Seek Harness for Powerful LASER Light," *Bakersfield Californian*, Jun. 3, 1963. Available: https://newspaperarchive.com/bakersfield-californian-jun-03-1963-p-5/

[2] G. D. Hickman and J. E. Hogg, "Application of an airborne pulsed laser for near shore bathymetric measurements," *Remote Sensing of Environment*, vol. 1, no. 1, pp. 47–58, 1969. Available: https://www.sciencedirect.com/science/article/abs/pii/S0034425769900881/

[3] C. Mobley, Light and Water: Radiative Transfer in Natural Waters. Academic Press, 1994.

[4] J. T. O. Kirk, *Light and Photosynthesis in Aquatic Ecosystems*. Cambridge, UK: Cambridge University Press, 1983.

[5] T. J. Petzold, "Volume scattering functions for selected ocean waters," Naval Air Development Center, 1972. Available: https://escholarship.org/uc/item/73p3r43q

[6] J. M. Sullivan, J. R. Twardowski, C. Moore, A. Barnard, P. L. Donaghay, and B. Rhoades, "The hyper-spectral temperature and salinity dependent absorption of pure water, salt water and heavy salt water(D 2 O) in the visible and near-IR wavelengths (400 - 750 nm)," *App. Opt.*, vol. 45, no. 21, pp. 5294–5309, 2006. Available: https://www.researchgate.net/publication/6959523_Hyperspectral_temperature_and_salt_dependencies_of_absorption_by_water_and_heavy_water_in_the_400-750_nm_spectral_range/

[7] A. Morel, "Optical modeling of the upper ocean in relation to its biogenous matter content (case 1 waters)," *J. Geophys. Res.*, vol. 93, no. C9, pp. 10749–10768, Sep. 1988. Available: https://agupubs.onlinelibrary.wiley.com/doi/10.1029/JC093iC09p10749/

[8] R. M. Measures, *Laser Remote Sensing: Fundamentals and Applications*. Malabar, FL, USA: Krieger Publishing Company, 1992.

[9] D.-M. He and A. Asundi, "Optical breakdown laser-generated sound in water," *SPIE*, Oct. 1998. Available: https://spie.org/Publications/Proceedings/Paper/10.1117/12.323152/

[10] S. Geng, H. Zheng, Z. Yao, Q. Zhong, and F. Wang, "Early dynamics of a laser-induced underwater shock wave," *J. Fluid. Eng.*, vol. 144, Jan. 2022. Available: https://asmedigitalcollection.asme.org/fluidsengineering/article-abstract/144/1/011501/1109936/Early-Dynamics-of-a-Laser-Induced-Underwater-Shock/

[11] B. Neuner, "National Information Warfare Center Data," National Information Warfare Center. 2023.

[12] J. H. Smart, "World-wide Ocean Optics Database (WOOD) 1900-2011 (NCEI Accession 0092528)," Applied Physics Laboratory. 2012. Available: https://www.ncei.noaa.gov/archive/accession/0092528/

[13] R. Olsen, interview, Feb. 2023.

INITIAL DISTRIBUTION LIST

1. Defense Technical Information Center
   Ft. Belvoir, Virginia

2. Dudley Knox Library
   Naval Postgraduate School
   Monterey, California